Permian-Triassic red-stained albitized profiles in the granitic basement of NE Spain: evidence for deep alteration related to the Triassic palaeosurface

Carles Fàbrega, David Parcerisa, Médard Thiry, Christine Franke, Andrey Gurenko, David Gòmez-Gras, Jesús Solé, Anna Travé

Permian-Triassic red-stained albitized profiles in the granitic basement of NE Spain: Evidence for deep alteration related to the Triassic palaeosurface

Carles Fàbrega[a], David Parcerisa[a,*], Médard Thiry[b], Christine Franke[b], Andrey Gurenko[c], David Gòmez-Gras[d], Jesús Solé[e,f], Anna Travé[g]

[a] *Departament d'Enginyeria Minera, Industrial i TIC, Escola Politècnica Superior d'Enginyeria de Manresa (UPC – Campus Manresa), Av. Bases de Manresa, 61-73, 08242, Manresa.*

[b] *MINES ParisTech, PSL Research University, Center of Geosciences, 35 rue St. Honoré, 77305, Fontainebleau, Cedex, France.*

[c] *Centre de Recherches Pétrographiques et Géochimiques, UMR 7358, Université de Lorraine, 15 rue Notre-Dame des Pauvres, BP 20, 54501 Vandoeuvre-lès-Nancy, France.*

[d] *Departament de Geologia, Edifici C, Universitat Autònoma de Barcelona, 08193 Bellaterra, Spain.*

[e] *Instituto de Geología, Universidad Nacional Autónoma de México, Ciudad Universitaria, Coyoacán, 04510 México DF, México*

[f] *Laboratorio Nacional de Geoquímica y Mineralogía, Universidad Nacional Autónoma de México, Ciudad Universitaria, Coyoacán, 04510 Mexico DF, Mexico*

[g] *Departament de Geoquímica, Petrologia i Prospecció Geològica, Facultat de Geologia. Universitat de Barcelona. Zona Universitària de Pedralbes, 08028 Barcelona*

* *Corresponding autor: David Parcerisa. E-mail: dparcerisa@epsem.upc.edu*

Tel.:+34 938 777 991

ABSTRACT

Extensive areas of the Variscan granitic basement in NE Spain display profiles of red-stained albitized facies characterized by albitization of Ca-plagioclase, chloritization of biotite and microclinization of orthoclase, along with the alteration of igneous quartz to secondary CL-dark quartz. These profiles have a geopetal structure beneath the Triassic unconformity, with a very intense and pervasive alteration in the upper part that progressively decreases with depth to 150-200 m where the alteration is restricted to the walls of fractures. The red albitized facies contains secondary maghemite and hematite that indicate oxidizing conditions. Dating of microclinized orthoclase and secondary monazite that have formed in the red-stained albitized facies yielded K-Ar and U-Th-Pb_{total} ages of 240 and 250 Ma, respectively, suggesting that the alteration developed during the Permian-Triassic period. The geopetal disposition of the red albitized profile with respect to the Triassic unconformity, its large regional extent, and the fracture-controlled alteration in the lower part of the profile indicate groundwater interaction. The $\delta^{18}O$

values of albitized plagioclase (+11‰), microclinized orthoclase (+13‰), and secondary CL-dark quartz (+12‰), suggest that the alteration temperature was about 55ºC. This "low" temperature suggests that the alteration occurred during interaction of the granitic rocks with Na-rich fluids below a surficial weathering mantle on the Permian-Triassic palaeosurface. The latter is possibly related to Triassic evaporitic environments in long-lasting, stable landscapes in which Na-rich solutions infiltrated deep regional groundwaters.

Keywords: red-stained; albitization; alteration; Permian-Triassic; palaeosurface; isotope; dating;

Introduction

Albitization of Ca-plagioclase is a widespread replacement process described in sedimentary deposits (Coombs, 1954; Kastner and Siever, 1979; Ramseyer et al., 1992) and crystalline rocks (Baker, 1985; Lee and Parsons, 1997; Parsons and Lee, 2009; Plümper and Putnis, 2009; Parsons et al., 2009; Morad et al., 2010; Petersson et al., 2012, 2014; Fallourd et al., 2014). It is a marker for the interaction of the respective facies with Na-rich brines and has been described as occurring over a wide temperature range from 65 to 160ºC in basinal settings (Boles, 1982; Saigal et al., 1988) and between 200 and 400ºC in hydrothermal conditions (Petersson and Eliason, 1997; Boulvais et al., 2007; Poujol et al., 2010). Usually, depths from 2 to 4 km are reported for current and fossil albitization processes in sedimentary basins and geothermal fields (Aagaard et al., 1990; Morad et al., 1990; Perez and Boles, 2005).

Extensive ~150 to 200 m thick vertical profiles characterized by red-staining and albitization of the crystalline basement have been described beneath the Triassic unconformity in various parts of Western Europe. In many cases a Permian-Triassic age has been stablished for them by direct (radiometric and paleomagnetic dating) or indirect evidences (geological cartography). Significant occurrences of the red-stained albitized profiles have been reported in the French Massif Central, including some affecting Carboniferous and Permian deposits (Yerle and Thiry, 1979; Clément, 1986; Schmitt, 1986, 1992; Schmitt et al., 1984; Simon-Coinçon, 1999; Thiry et al., 1999, 2014), the Morvan Massif (Ricodel et al., 2007; Parcerisa et al., 2010b), the Alps (Battiau-Queney, 1997), the Polish Sudetes (Yao et al., 2011; Yao, 2013) and the Spanish Guilleries and Roc de Frausa Massifs (Fàbrega et al., 2013; Franke et al., 2010; Parcerisa et al., 2010a; 2013). Away from the above sites, the age of granite albitization and even red-staining have rarely been documented. However, a profile-like alteration diminishing in intensity with depth and characterized by reddening by hematite and accompanying recrystallization of feldspars has been reported in the Long Mountain Granite of the Wichita Mountains igneous province, southwestern Oklahoma (Hamilton et al., 2014, 2016). This alteration is considered to have been caused by low-temperature weathering fluids while the granite was exposed near the surface in the late Palaeozoic.

The present study focusses on the spatial distribution, geometry, petrology, age and oxygen isotope composition of the red-stained albitized profiles in the Variscan granitic basement beneath the Triassic unconformity of the Guilleries and Roc de Frausa massifs (NE Spain), with aims to: 1) determine the genetic relationship of the alteration with the Permian-Triassic palaeosurface, 2) constrain the age of the

alteration event, 3) evaluate the origin and temperature of the albitizing fluid, and 4) gain an understanding of subsurface processes that operated beneath the Triassic palaeosurface.

Geological setting and study sites

The granitic massifs of the Guilleries (Catalan Coastal Ranges) and Roc de Frausa (Eastern Pyrenees) form part of the Variscan crystalline basement of NE Spain (Fig. 1a, b) and are made up of late-orogenic batholiths intruded into the upper part of the crust (Roberts et al. 2000; Vilà et al. 2005; Aguilar et al. 2014, 2015). The Guilleries Massif consists of granodiorite, leucogranite and diorite bodies (Fig. 2a) that intruded a Cambro-Ordovician metamorphic series (Julivert and Duran, 1990; Enrique, 1990). The igneous and metamorphic rocks are cross-cut by a swarm of ENE-WSW trending vertical dikes of granitic to monzonitic composition. Martínez et al. (2008) reported bimodal cooling ages of 305.9 ± 1.5 and 323.6± 2.8 Ma from U-Pb dating of zircon in, respectively, biotite granites and diorite bodies. In the south of the massif and in the Tagamanent area the crystalline basement is covered by Middle Triassic (Anisian) red-beds (Fig. 2a, b) that were deposited in the Permian-Triassic rift basins of northeastern Spain (Solé de Porta et al., 1987; Dinarès-Turell et al., 2005; Gómez-Gras, 1993). In the north (Fig. 2a), the unconformity is covered by Palaeocene red-beds deposited in the eastern boundaries of the Ebro Basin (Anadón et al., 1986).

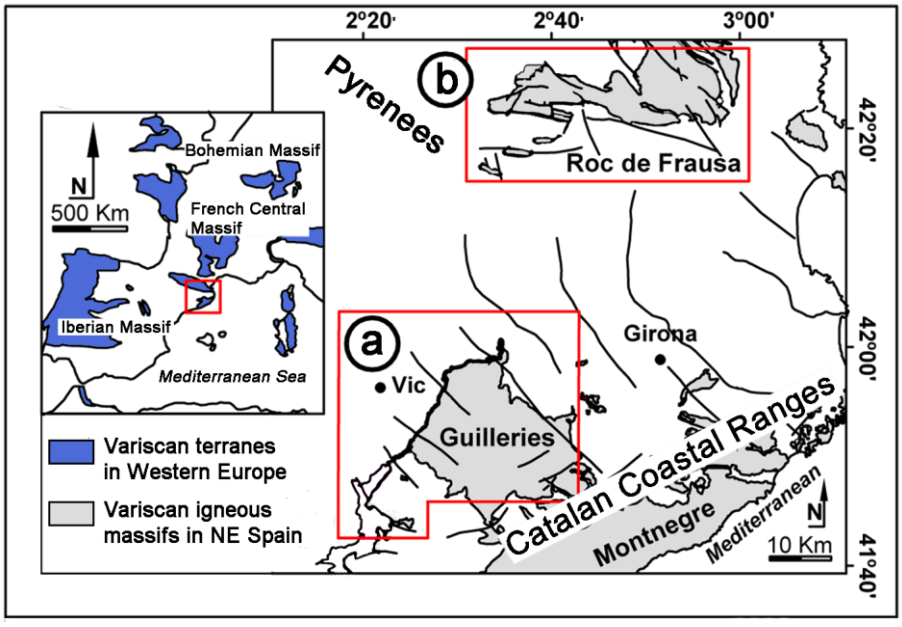

Fig. 1. Location of the Guilleries **(a)** and Roc de Frausa **(b)** massifs in the Variscan terranes of the Catalan Coastal Ranges and Eastern Pyrenees.

The igneous basement of the Roc de Frausa Massif is formed of biotite-hornblende granite, granodiorite, leucogranite, monzo-granite, and porphyritic granites (Fig. 2c) that intruded a Proterozoic to early Cambrian sequence of metapelites, ortho-gneiss, and metagreywackes (Aguilar et al., 2015). To the southwest, the areas of Hortmoier, Oix and St. Aniol are made up of porphyrytic granite with K-feldspar phenocrysts (Fig. 2c). U-Pb dating of zircons yielded two cooling episodes for the granites corresponding to 314.2 ± 1.5 and 311.0 ± 0.9 Ma (Aguilar et al., 2014). The sedimentary cover is formed of south-tilted (40-50º) Upper Cretaceous (Maastrichtian) red-beds (Oms et al., 2007; Gómez-Gras et al., 2016).

In the Guilleries Massif, the red-stained albitized granitoids crop out along the Triassic unconformity, which is situated in the western boundary of the massif (Fig. 2a). The rocks affected by the red-stained albitization are exposed in a total area about 20 km long by 2-3 km wide in a N-S direction (Fig. 2a). In the Tagamanent area (Fig. 2b), the red-stained albitized granites crop out between 1100 to 900 meters above sea level in a topography-related ~200 m thick profile beneath the Triassic unconformity.

In the Roc de Frausa Massif, the red-stained albitized rocks are exposed along the Triassic unconformity in the southern limit of the massif (Fig. 2c). The total area affected by albitization is about 25 km long by ~2 km wide in an E-W direction (Fig. 2c). In the areas of Oix, Hortmoier and St. Aniol (Fig. 2c), the red-stained albitized rocks also occur along the Triassic unconformity situated in the southern limit of the three areas.

The study sites in both massifs (Table 1) focussed on the red-stained albitized granitoids cropping out under the Triassic unconformity and on their unaltered counterparts (Fig. 2a, b, c). Several cross sections were constructed to determine the structure and depth of the red-stained albitization with respect to the Triassic unconformity (Fig. 2d, e). Further detailed information on the study sites is included in the **Supplementary Information S1**, available at the dataset of Fàbrega et al. (2018).

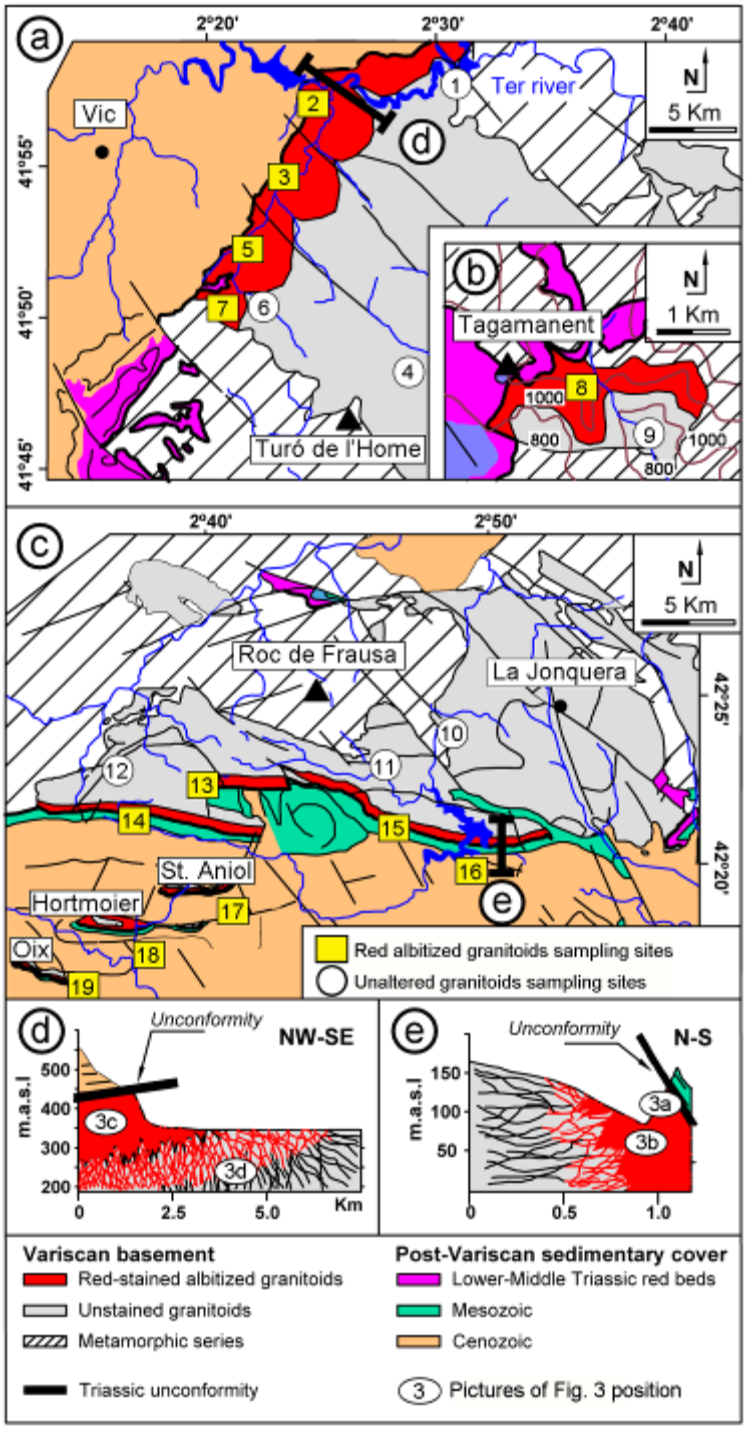

Fig. 2. Geological setting, sampling sites and cross-sections. **(a)** Guilleries Massif. **(b)** Tagamanent hill, located on the south of the Guilleries Massif. **(c)** Roc de Frausa Massif, St. Aniol, Hortmoier and Oix. **(d)** Sau dam cross section. **(e)** Boadella dam cross section. **Main sampling sites**: Guilleries Massif: (**1**) Susqueda dam; (**2**) Sau dam; (**3**) Bojons; (**4**) Arbúcies and St. Coloma de Farners; (**5**) Osormort; (**6**) Viladrau; (**7**) Mas Vidal-Timonar; (**8**) Tagamanent; (**9**) Vallfornès. Roc de Frausa Massif: (**10**) La Vajol; (**11**) Maçanet de Cabrenys; (**12**) St. Laurent Cerdans; (**13**) Coustoges; (**14**) Villerouge; (**15**) Puig Creu de Mondavà; (**16**) Boadella dam; (**17**) St. Aniol; (**18**) Hortmoier; (**19**) Oix.

Methods and materials

The analytical data for this study are included in **Supplementary Information S2** and **S3** and are available also in the institutional repository [dataset] Fàbrega et al. (2018).

Sampling and mapping

Sampling, mapping and construction of cross-sections of the red albitized granitoids were systematically carried out along the Triassic unconformity of both massifs (Fig. 2). Due to a dense forest cover in most of the study areas, the work was mostly carried out along linear features including roads, trails and creeks. A total of about 280 and 100 samples were collected in the Guilleries and Roc de Frausa Massifs, respectively, including pervasively albitized rocks, albitization restricted to fractures and unaltered rocks (Table 1).

Table 1. Sampling sites, their numbering in Figure 1, nature of the host rocks and their alteration features.

massif	sampling sites	N. in (Fig. 1)	host rock	samples major features
Guilleries	Susqueda dam	1	granodiorite	unaltered
	Sau dam	2	leucogranite	pervasive red albitized
	Bojons	3	granodiorite + dikes	pervasive red albitized
	Arbúcies / St. Coloma	4	granodiorite + leucogranite	red albitized fracture walls
	Osormort	5	granodiorite + dykes	pervasive red albitized
	Viladrau	6	granodiorite	unaltered
	Mas Vidal-Timonar	7	granodiorite + dykes	pervasive red albitized
	Tagamanent	8	porphyritic granite	pervasive red albitized
	Vallfornès	9	porphyritic granite	unaltered
Roc de Frausa	La Vajol	10	hornblende-biotite granodiorite	unaltered
	Maçanet de Cabrenys	11	hornblende-biotite granodiorite	unaltered
	St. Laurent Cerdans	12	hornblende-biotite granodiorite	unaltered
	Coustoges	13	porphyritic granite	pervasive red albitized
	Villerouge	14	porphyritic granite	pervasive red albitized
	Puig Creu Mondavà	15	porphyritic granite	pervasive red albitized
	Boadella dam	16	porphyritic granite	pervasive red albitized + unaltered
	St. Aniol	17	porphyritic granite	red albitized fracture walls
	Hortmoier	18	porphyritic granite	red albitized fracture walls
	Oix	19	porphyritic granite	red albitized fracture walls

Petrological and geochemical analyses

About 80 samples were prepared as thin sections and epoxy-embedded mounts for petrographical analyses. Samples were observed by optical microscopy and optical cathodoluminescence (CL) using a Technosyn Cold Cathodoluminescence 8200-MKII-CL operating at 15-18 kV gun potential and 150 - 350 µA beam current at the Facultat de Ciències de la Terra of the Universitat de Barcelona (Spain). The quality of the CL-microphotographs was improved by following the recommendations of Witkowski *et al.* (2000). SEM-cathodoluminescence (SEM-CL) of quartz was undertaken using a FESEM JEDL J-7100 equipped with a GATAN MONO-CL4 cathodoluminescence spectrometer at the Centres Científics i Tecnològics (CCiTUB) of the Universitat de Barcelona (Spain). The textural features of quartz under SEM-CL were analysed according to the techniques of Bernet and Basset (2005), Rusk and Reed (2002) and Rusk et al. (2006).

The chemical composition of bulk rock was determined by laser X-ray fluorescence (LXRF) at the Instituto de Geología of the Universidad Nacional Autónoma de México (México) using a Rigaku Primus II spectrometer. Detailed chemical composition of minerals was determined by electron probe microanalyses (EPMA) using a JEOL JXA-8230 instrument at the Centres Científics i Tecnològics (CCiTUB) of the Universitat de Barcelona (Spain). The operating conditions were acceleration voltage of 20 kV and probe current of 1.5 nA. The surfaces of thin sections and epoxy mounts used in EPMA analyses were polished metallographically. EPMA analyses were carried out on several kinds of granitoids, including leucogranite and granodiorite in the Guilleries and porphyritic granite in the Roc de Frausa and on similar red-stained albitized rocks. In total about 1400 spots were analysed.

The degree of microclinization of 73 K-feldspar phenocrysts was quantified by X-ray diffraction (XRD) at the Center of Geosciences, Mines ParisTech, Fontainebleau (France). Identification of the orthoclase, microcline and albite was carried out by peak deconvolution using the *Fityk* software (Wojdyr, 2010) adjusting the shape of the deconvoluted peaks by the Pearson VII function (Hall et al., 1977). The position of the peaks was calibrated with respect to the quartz peaks, which are present in the samples.

K-Ar dating of K-feldspar phenocrysts was carried out at the Instituto de Geología of the Universidad Nacional Autónoma de México. The analyses were done on 1 unaltered and 7 pinkish phenocryst subsamples from Hortmoier (see Fig. 2). Fragments of the K-feldspar phenocrysts about 2-5 mm in size were hand-picked with the aid of a stereo microscope. The selected fragments were cleaned with distilled

water and acetone. The K content was measured by XRF on 50 mg aliquots using a specific regression for measuring K in K-Ar samples (Solé and Enrique, 2001). Analytical precision was > 2%. Duplicate samples weighing between 1 and 2 mg were mounted on holes of a copper plate. This plate was placed on an ultra-high vacuum chamber that was degassed at ~150°C for twelve hours before analysis to reduce atmospheric contamination. Argon was extracted by complete sample fusion using a 50 W CO_2 laser defocused to 1 - 3 mm diameter. The evolved gasses were mixed with a known amount of ^{38}Ar spike and purified with a cold finger immersed in liquid nitrogen and two SAES getters in a stainless-steel extraction line. Measurements were done in static mode with an MM1200B noble gas mass spectrometer using electromagnetic peak switching controlled by a Hall probe. Analytical precision on ^{40}Ar and ^{38}Ar peak heights was better than 0.2%, and better than 0.5% for ^{36}Ar. The data were calibrated with internal standards and the international reference materials LP-6 biotite, B4M muscovite and HD-B1 biotite. All ages were calculated using the constants recommended by Steiger and Jäger (1977). A detailed description of the procedure and calculations is given by Solé (2009).

U-Th-Pb_{total} EPMA monazite dating

Monazite geochronology was carried out by EPMA U-Th-Pb_{total} dating following the recommendations of Cocherie et al. (1998), Cocherie and Albarede (2001) and Williams et al. (2006). The technique assumes a negligible amount of common vs. radiogenic Pb (Parrish, 1990), very slow Pb diffusion (Cherniak et al., 2004; Cherniak and Pyle, 2008) and the complete removal of prior Pb during the formation of secondary monazite domains, thus resetting the U-Th-Pb_{total} chemical geochronometer (Williams et al., 2011).

Monazite grains were first identified in the thin sections by means of BSE imaging in a Hitachi TM-1000 electron microscope operating at 15 kV at the Escola Politècnica Superior d'Enginyeria de Manresa (EPSEM) of the Universitat Politècnica de Catalunya (Spain). The U-Th-Pb_{total} EPMA analyses were carried out using a JEOL JXA-8230 electron probe operating at 20 kV at the Centres Científics i Tecnològics (CCiTUB) of the Universitat de Barcelona (Spain). The session-to-session consistency of the EPMA analyses was controlled using an in-house monazite standard from Coats pegmatite (Petaca district, New Mexico). The reference U-Th-Pb isotopes standard age was 1332.6 ± 4.6 Ma (2σ), obtained by LA-ICP-MS at Geosciences Rennes, Université de Rennes 1 (France). The U-Th-Pb_{total} ages of the standard obtained in each EPMA session were, respectively, 1313 ± 30, 1307 ± 36, 1308 ± 44, and

191 1305 ± 32 Ma (2σ), being consistent, within 2σ, with the U-Pb and Th-Pb age obtained by laser ablation
192 coupled with MC-ICP-MS.

193 In the unaltered igneous rocks, primary monazite occurred as euhedral (20 - 50 µm) or rounded (usually
194 150 - 200 µm) grains that did not show internal BSE-zoning. In the red-stained albitized granitoids,
195 monazite is exclusively preserved in a mm-scale rock volume attached to the reaction front. In this
196 volume, monazite is pseudomorphosed by secondary monazite and apatite, and displays dissolution-
197 reprecipitation textures including corroded grain boundaries and widespread µm-size porosity (Putnis,
198 2002; Harlov et al., 2011).

199 The analyses were performed on three representative samples of unaltered rock and two representative
200 samples plus 2 subsamples of red albitized rock. A total of 530 spots were analysed. Afterwards, the
201 EPMA raw U-Th-Pb_{total} results presenting a sum of oxides less than 95% and/or a relative standard
202 deviation of U and/or Th and/or Pb larger than 20% were rejected. Finally, 117 and 80 analyses were used
203 to estimate the U-Th-Pb ages for the Guilleries and Roc de Frausa, respectively. The U-Th-Pb_{total} dates of
204 the individual EPMA points were calculated using the *MonaziteAge* software included in the JEOL JXA-
205 8230 electron probe, which uses the approach of Suzuki and Adachi (1991, 1994) and Suzuki et al.
206 (1994). Subsequently, the standard error of each single date was estimated using the Microsoft Excel
207 (Microsoft Inc.) add-in *EPMA dating 2007* developed by A. Pommier, A Cocherie and O. Legrenge at the
208 BRGM. The final U-Th-Pb_{tot} ages of the primary and secondary monazite were calculated by
209 deconvolution of the histograms of the punctual U-Th-Pb_{total} dates using the Microsoft Excel add-in
210 *ISOPLOT 4.15* from the Berkeley Geochronology Center (Ludwig, 2003).

211 ### *In-situ* $\delta^{18}O$ SIMS analyses

212 In-situ $\delta^{18}O$ (to VSMOW) SIMS analyses of plagioclase, K-feldspar and quartz were carried out using a
213 CAMECA IMS 1280HR ion microprobe at the Centre de Recherches Pétrographiques et Géochimiques,
214 Centre National de la Recherche Scientifique (Nancy, France). Rock samples were cut into 4×4×4 mm
215 pieces, mounted in cylindrical 25 mm diameter/5 mm thick epoxy mounts accompanied by mm-sized
216 fragments of in-house feldspar and quartz standards and metallographically polished. Optical-CL
217 microphotographs of the surfaces of samples and standards were obtained and were subsequently used
218 during the SIMS session to locate the oxygen isotope analyses on the desired textural position. The SIMS
219 analyses were carried out using a $^{133}Cs^{+}$ primary ion beam of +10 kV and intensity of 5 – 6 nA. Vacuum

conditions in the sample chamber were about ~E^{-9} Torr. Positive charging of the sample surface was prevented by means of a gold coating and a normal incident electron flood gun. Secondary negative ions were accelerated by a 10 kV potential. After pre-sputtering, the secondary ion beam was automatically centered onto the field aperture by the electrostatic deflectors LT1DefX and LT1DefY. The produced $^{16}O^-$ and $^{18}O^-$ were simultaneously collected in multicollection mode using two Faraday cups (FC; L'2 for counting $^{16}O^-$ ions, and H1 for $^{18}O^-$ ions). Each single analysis included 30×5-s-long counting cycles, with a total span time of ~4 min, including 60 s of pre-sputtering.

The in-house standards used for the correction of the SIMS instrumental mass fractionation (IMF) included eight plagioclase, two K-feldspar and one quartz specimens. The textural characteristics, chemical and bulk $\delta^{18}O$ compositions of the in-house standards are described in Fàbrega et al. (2017) and hosted in the institutional repository *UPCommons* of the Universitat Politècnica de Catalunya, Spain (Parcerisa et al., 2016). The averaged internal precision (within-spot uncertainty) of the standards analyses was 0.06‰ (1σ) for the whole session. The external precision (spot-to-spot reproducibility) was in the range 0.29 - 0.5‰ (1σ). Mount-to-mount reproducibility was 0.29‰ (1σ), estimated as the standard deviation of four $\delta^{18}O$ values, and obtained by averaging sets of five analyses of a K-feldspar standard ($\delta^{18}O$ = 9.3 ± 0.1‰, 1σ) in four different mounts during the session.

The IMF of the plagioclase, K-feldspar and quartz $\delta^{18}O$ SIMS analyses were predicted by response surface methodology (RSM) using the three response surface models described in Fàbrega et al. (2017). The predictor (input) variables were the instrumental parameters X and Y stage position, primary beam intensity (PI), chamber pressure (CP) and, electrostatic deflectors LT1DefX and LT1DefY. In addition, the models for feldspars included the compositional inputs An% (plagioclase model) and Or% and BaO% (K-feldspar model). The IMF was considered as the predicted (output) variable or response. This RSM approach permitted to predict a unique IMF value for each SIMS analysis.

The SIMS $\delta^{18}O$ analyses of unaltered rock were carried out on 2 samples in Guilleries and 2 samples in the Roc de Frausa. On red-stained albitized rock, $\delta^{18}O$ analyses were also performed on 2 samples in Guilleries and 2 samples in Roc de Frausa. A total of 54 and 90 $\delta^{18}O$ SIMS analyses were carried out on the Guilleries and Roc de Frausa samples, respectively.

Structure and petrology of the alteration

Unaltered facies

The unaltered facies of the Guilleries consists of granodiorite and leucogranite. Primary Ca-plagioclase occurs as euhedral 1 – 3 mm zoned crystals with polysynthetic twinning and yellow-green luminescence. Ca-plagioclase grains have compositions in the core and rim of, respectively, Ab_{79-90} and Ab_{89-99} in the leucogranite and Ab_{60-90} and Ab_{92-99} in the granodiorite (Table 2). Primary K-feldspar is orthoclase characterized by subhedral 0.5 - 3 mm crystals with micro and crypto perthite lamellae, blue luminescence and a chemical composition in the range Or_{84-96} for both the leucogranite and the granodiorite (Table 2). The porphyritic granite of the Tagamanent area (see Fig. 2b) has white orthoclase phenocrysts (2 - 3 cm) with blue luminescence containing micro and crypto perthite lamellae. Quartz occurs as 0.1 – 2 mm anhedral grains with homogeneous grey SEM-CL and cooling microcracks. Biotite occurs as brown to green 0.1 – 3 mm tabular grains with an Fe/Fe+Mg ratio ranging from 0.82 - 0.84 and 0.61 - 0.70 for the leucogranite and the granodiorite, respectively. The accessory minerals are zircon, epidote, apatite-(F), monazite-(Ce) and xenotime. Zircon occurs as 10 – 50 µm zoned euhedral crystals, epidote as euhedral 10 – 30 µm elongated crystals, and apatite as 5 – 20 µm rounded crystals within biotite. Monazite is typically 20 – 50 µm euhedral or rounded grains that commonly reach 200 – 300 µm in size. Xenotime mostly forms euhedral 30 – 50 µm crystals. Magnetite (Fe_3O_4) is the dominant ferromagnetic mineral in the unaltered igneous rocks of the Guilleries Massif (Franke et al., 2010).

The unaltered facies in Roc de Frausa is mainly porphyritic granite with K-feldspar phenocrysts (2–3 cm), and this also occurs in the St. Aniol, Hortmoier and Oix areas (Fig. 2c). Primary Ca-plagioclase occurs as zoned euhedral 0.5 – 2 mm crystals with polysynthetic twinning, yellow-green luminescence and a composition in the ranges Ab_{66-74} and Ab_{90-99} for the Ca-rich cores and the Na-rich zones, respectively (Table 2). The matrix K-feldspar is subhedral to euhedral 0.5 – 2 mm crystals with micro- and crypto perthite lamellae, blue luminescence and a composition of Or_{74-98} (Table 2). The K-felspar phenocrysts (2 – 3 cm) are white orthoclase with blue luminescence, a composition in the range Or_{70-90}, and micro and crypto perthite lamellae. Quartz is present as 0.5 – 3 mm anhedral crystals with homogeneous SEM-CL and cooling microcracks. Biotite usually occurs as 1 - 3 mm tabular crystals with a Fe/Fe+Mg ratio in the range 0.61 - 0.65. The accessory minerals are euhedral 10 – 50 µm zircon, 5 – 15 µm rounded apatite-(F),

euhedral 10 – 30 µm epidote, euhedral or rounded 20 – 40 µm monazite-(Ce), and occasional euhedral 20 – 50 µm xenotime.

Red-stained albitized facies

The red-stained albitized facies beneath the Triassic unconformity has the form of a ~150-200 m deep geopetal structure characterized by a decreasing intensity of alteration from the top to the bottom (Fig. 2d, e). The alteration in the upper part is very pervasive and the rock is a red facies (Fig. 3a). The degree of alteration progressively decreases with depth and the rock is a pink facies in the intermediate zone of the profile (Fig. 3b, c). In the lower part of the profile, the red-stained albitization is restricted to the walls of fractures and the rock presents as a 'spotted' facies (Fig. 3d, 3e). The fractures controlling alteration in the lower parts of the profile are likely to have developed by pre-existing cooling and decompression of the granitic mass. In the upper part of the profile, closer to the unconformity, more pervasive alteration was accomplished via a greater abundance of joints and fractures together with micro-fractures and grain boundaries penetrating the matrix of the rock. Here, effective fluid pathways could also have progressively self-generated through reaction-induced hierarchical fracturing (Røyne et al., 2008; Jamtveit et al., 2009).

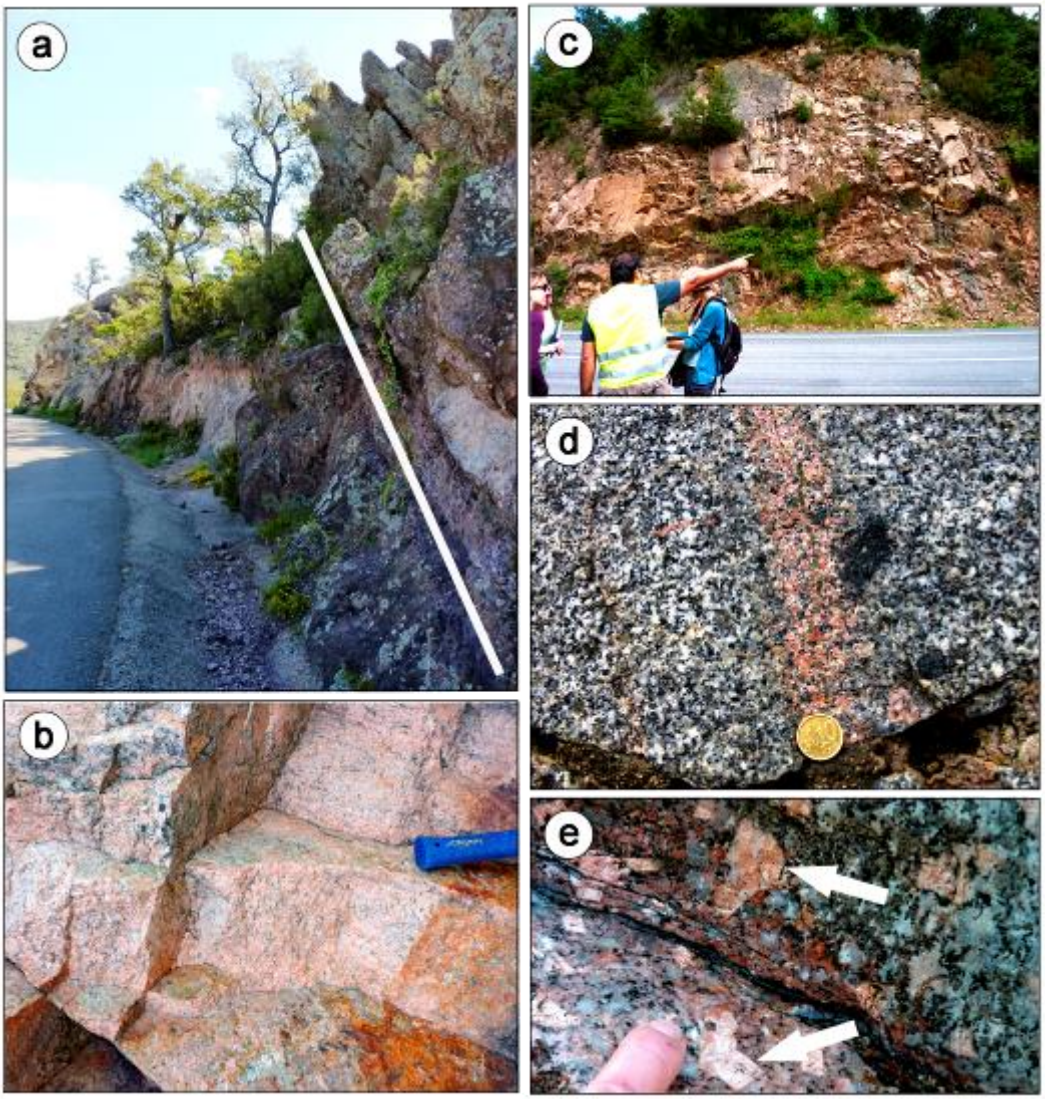

Fig. 3. Red stained albitized facies. **(a)** Red albitized porphyritic granite (lower left) unconformably overlain by south-dipping Upper Cretaceous (Maastrichtian) red-beds (upper right). Boadella dam, Roc de Frausa massif. **(b)** Pervasively albitized pink porphyritic granite near the top of the profile. Boadella dam, Roc de Frausa massif. **(c)** Completely albitized red - pink granodiorite in the upper part of the profile. Mas Vidal area, Guilleries massif. **(d)** Red albitization along fractures (coin) through unaltered granite in the bottom of the profile. Sau dam, Guilleries massif. **(e**) Red albitization along fractures including microclinized pink orthoclase phenocrysts (white arrows) in the lower part of the profile. Hortmoier area.

The nature of Fe-oxides evolves within the profile. Hematite (Fe_2O_3) dominates in the red facies of the upper part of the profile (Fig. 4), indicating stronger oxidizing conditions. Hematite crystals are micron-sized and occur inside the microporosity of secondary feldspars, suggesting that they formed by fluid-rock interaction rather than feldspar exsolution (Putnis et al., 2007). Hematite is considered to have formed by both the alteration of maghemite and authigenic precipitation. The composition of hematite in

the red facies is about $Ilmenite_{10}$ $Geikielite_{1}$ $Pyrophanite_{1}$ and $Hematite_{88}$, probably reflecting the introduction of Ti released during biotite chloritization into the hematite structure. The concentration of maghemite (γ-Fe_2O_3) increases with depth (Fig. 4), indicating progressively decreasing oxidizing conditions. Maghemite is considered to have formed by oxidation of primary magnetite and by authigenic precipitation at low temperature (Franke et al., 2010).

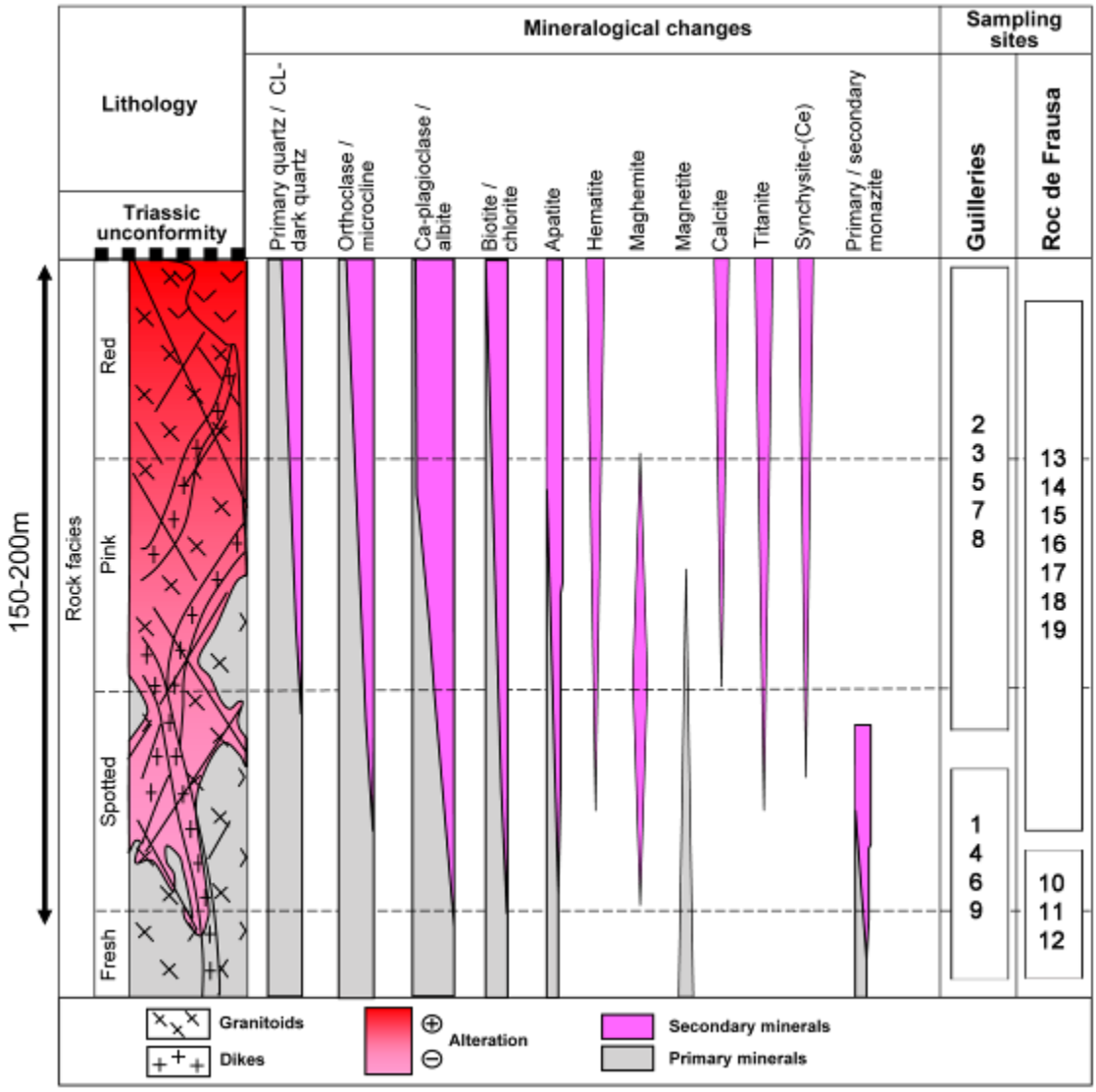

Fig. 4. Evolution of the albitized facies and the mineralogy of the profile. Numbers correspond to sampling sites presented in **Fig. 2**. Adapted from Yao (2013).

The reactions that affect the major minerals are albitization of Ca-plagioclase, chloritization of biotite, microclinization of orthoclase, and the alteration of igneous quartz to secondary CL-dark quartz (Fig. 4).

Primary Ca-plagioclase is pseudomorphosed by secondary albite. Albitized plagioclase grains (Fig. 5a, b, c) have a turbid aspect, a lack of luminescence, widespread micron-sized non-connected euhedral porosity (Fig. 5d) and a very pure chemical composition in the range of Ab_{97-99} (Table 2). The replacement front between the primary Ca-plagioclase and the secondary albite is very sharp (Fig. 5b), and the crystallographic framework is preserved from the primary to the secondary phase. These textural features are typical of a fluid-aided dissolution-reprecipitation process along micro-fractures without development of dissolution pores prior to precipitation (Putnis, 2002; Engvik et al., 2008; Putnis, 2009). The albitized plagioclase grains usually contain micron-sized non-luminescent secondary K-feldspar and orange-CL calcite (Fig. 5c), the latter with a composition about $Magnesite_{1.5}$ $Siderite_{0.7}$ $Calcite_{97.8}$. The primary green-yellow luminescent Na-rich rims of plagioclase, with the composition Ab_{90-93}, are preserved during albitization (Fig. 5a).

Primary biotite is pseudomorphosed by secondary chlorite. Chloritized biotite is non-luminescent, preserves the biotite sheet structure and usually contains lens-shaped inclusions of secondary K-feldspar, quartz and orange-CL calcite (Fig. 5c). The composition of the calcite inclusions formed inside chlorite is about $Magnesite_{2.4}$ $Siderite_{3.2}$ $Calcite_{94.3}$, reflecting a higher content of Mg and Fe released from primary biotite during chloritization than available to the calcite inclusions formed within secondary feldspars. The chloritized biotite grains systematically show a significant increase of yellow luminescent micron-sized fluorapatite inclusions (Fig. 5c). In places, neoformed chlorite occurs in sheaf like arrangements of micron-size sheets inside the micro porosity.

The microclinization of orthoclase is characterized by the recrystallization of primary orthoclase to secondary microcline. The microclinized grains have a cloudy aspect, loss of luminescence (Fig. 5a), a widespread micron-sized non-connected euhedral porosity, amoeboid-shaped patchy perthite texture and a composition of about Or_{96-99} and Or_{87-93} in the Guilleries and Roc de Frausa, respectively (Table 2). The patch perthite exclusively forms during the microclinization process and implies replacement of K-feldspar by secondary albite. K-feldspar phenocrysts (2 – 3 cm) in the porphyritic granites progressively change from the white color of the primary orthoclase to brown and finally red-pink as the degree of microclinization increases. The most strongly microclinized phenocrysts have a composition (XRD) of about 40 - 60% microcline, 20 - 30% albite and 10 - 40% orthoclase. The albite detected by XRD inside the red-pink phenocrysts includes the patch perthite and plagioclase inclusions that were albitized during microclinization.

The net of micro fractures in the red-stained albitized rocks is sealed by secondary CL-dark quartz that postdates the aforementioned reactions. Within quartz grains, this net of micron sized CL-dark quartz has a dendritic texture (Fig. 5e), suggesting that it propagated along sub-micron cracks and dislocations and may possibly record some degree of dissolution-reprecipitation process of the primary quartz.

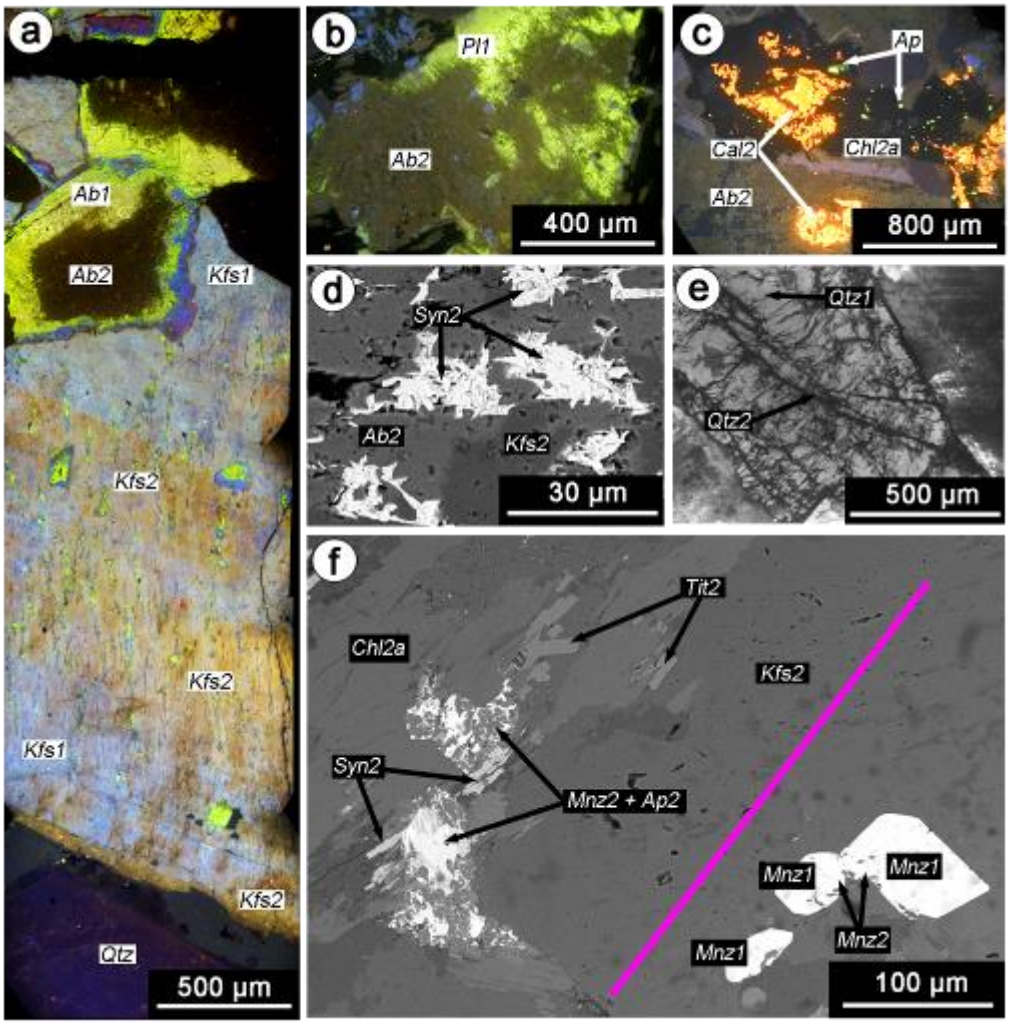

Fig. 5. Cathodoluminescence and SEM petrography of the albitized facies. **(a)** Pink albitized granite near the top of the profile. Albitized plagioclase grains display non-luminescent albitized cores (*Ab2*) and preserve a primary Na-rich CL-yellow rim (*Ab1*) in contact with a K-feldspar grain with primary CL-blue zones (*Kfs1*) and CL-turbid microclinized areas (*Kfs2*). **(b)** CL-yellow primary plagioclase (*Pl1*) partially pseudomorphosed by non-luminescent secondary albite (*Ab2*) penetrating along twin planes and micro fractures. **(c)** CL-image of very strongly albitized red granite at the top of the profile. Patches of secondary CL-orange calcite (*Cal2*) inside non-luminescent albitized plagioclase (*Ab2*) and chloritized biotite (*Chl2a*). Chloritized biotite also shows significant yellow apatite inclusions (*Ap*) compared with primary biotite. **(d)** BSE-image of clusters of synchysite-(Ce) 'sticks' inside the secondary

porosity of albitized plagioclase (*Ab2*) and microclinized orthoclase (*Kfs2*). **(e)** SEM-CL picture of igneous quartz grain from the upper part of the profile showing a dendritic net of CL-dark secondary quartz (*Qtz2*). Patches of primary quartz (*Qtz1*) are preserved. **(f)** BSE-image showing alteration of monazite in the reaction front approximately indicated by the pink line. Left, monazite pseudomorphosed by secondary monazite (*Mnz2*) and apatite (*Ap2*) and accompanied by euhedral synchysite (Syn2) and titanite (Tit2). Right, primary monazite grains (*Mnz1*) mostly preserved but showing some pseudomorphic secondary monazite (*Mnz2*) in the boundaries. *Chl2a*: Chloritized biotite; *Kfs2*: Microclinized orthoclase.

Authigenic synchysite-(Ce) [Ca(Ce, La)$(CO_3)_2$F] is the dominant REE-mineral in the red-stained albitized rocks (Fig. 4) and its abundance decreased from the top to the bottom of the profile. It usually occurs in clusters of 5-15 µm stick-shaped crystals inside the secondary micron-sized porosity of the albitized plagioclase, microclinized orthoclase and chloritized biotite (Fig. 5d), strongly suggesting coeval formation with these secondary minerals. Synchysite-(Ce) is mostly Th-poor (0 - 4.68 wt% Th $[CO_3]_2$) with 33 to 54 wt% of $LREE_2O_3$ and 1.6 to 5.5 wt% of Y_2O_3 + $HREE_2O_3$. The Ca content (wt. % $CaCO_3$) of Synchysite-(Ce) decreases from 29-32% at the top of the profile (n= 9) to 22-23% at the bottom (n= 10).

Monazite is strongly altered in the red and pink facies of the upper part of the profile, where the grains are completely pseudomorphosed by apatite and quartz inside a millimetre-scale zone adjacent to the reaction front (Fig. 5f). The secondary monazite shows evidence of dissolution-reprecipitation mechanisms including corroded boundaries, fracturing, and secondary micron-sized porosity (see for example Putnis, 2002, 2009). The pseudomorphosed monazite grains are usually accompanied by micron sized authigenic titanite, and synchysite (Fig. 5f).

The alteration of all silicates and non-silicates, namely albitization of Ca-plagioclase, microclinization of orthoclase, chloritization of biotite, and precipitation of secondary CL-dark quartz, iron oxides and REE-minerals, decreases from the top to the bottom of the profile (Fig. 4). In the same context, the succession of mineral alteration adjacent to fractures decreases in intensity towards the cores of the granite blocks. Decimetre-thick alteration zones occur adjacent to the major fractures, with restricted millimetre-thick zones walls adjacent to secondary fractures, and less along micro-cracks. These relationships point clearly to the influence of fluid circulation. As well, albitization was not associated with a volume change, i.e. the texture and fabric of the altered rocks is not significantly different from that of the unaltered rocks, at least at a macroscopic level.

Table 2. Representative composition of feldspars in the Guilleries and Roc de Frausa Massifs

	unaltered rock			red albitized rock	
massif	**plagioclase core (n= 86)**	**plagioclase rim (n= 100)**	**k-feldspar (n= 57)**	**albitized plagioclase (n= 95)**	**microclinized k-feldspar (n=126)**
Guilleries	Ab_{60-90}	Ab_{89-99}	Or_{84-96}	Ab_{97-99}	Or_{96-99}
Roc de Frausa	Ab_{66-74}	Ab_{90-99}	Or_{74-98}	Ab_{97-99}	Or_{87-93}

Geochemical characteristics of the alteration

Mass balance

The evaluation of element mobility during fluid-rock interaction can be referred to an "immobile" geochemical framework (Ague and van Haren, 1996). This is usually undertaken using one or more ostensibly immobile elements that are ideally concentrated in minerals that do not change during fluid-rock interaction and that present a low analytical uncertainty (Beinlich et al., 2010).

To estimate the mass changes caused by albitization (Table 3), the concentrations of the elements in the albitized rock samples were recalculated with respect to Zr, considered as an immobile reference. Petrographic observations show that zircon grains in the albitized rocks remain mostly unchanged from those in the unaltered facies.

Table 3. Mass balance between the unaltered and red-stained albitized rocks.

		averaged major elements concentrations (wt. %)									
rock	**n**	**CaO**	**K_2O**	**P_2O_5**	**TiO_2**	**Fe_2O_3**	**MnO**	**Al_2O_3**	**SiO_2**	**MgO**	**Na_2O**
unaltered	4	2.67	4.18	0.14	0.49	3.64	0.08	15.96	66.91	1.27	2.83
red albitized	3	1.06	2.38	0.12	0.46	3.63	0.08	17.01	78.41	1.64	5.40
variation %		-60	-43	-19	-5	-0.3	-2	+7	+17	+29	+91

Petrographical observations of the red-stained albitized rocks show that albitization of plagioclase, microclinization of K-felspar, and chloritization of biotite are intimately linked to the precipitation of secondary synchysite-(Ce), apatite, epidote, calcite and hematite that probably recycled some of the ions released by the major reactions. Consistent with the albitization of primary plagioclase, the amount of Na in the albitized rock presents a mass increase of about +91%, and a Ca loss of -60% (Fig. 6). By considering the atomic mass of Na and Ca, this means that only about half of the Ca released by replacement of plagioclase by albite has been removed from the system. The remnant Ca was likely

recycled into secondary synchysite-(Ce), apatite, epidote, and calcite. The K content presents a significant reduction of -43% (Fig. 6), which is consistent with the systematic biotite chloritization and some K-feldspar albitization. A fraction of the K is probably retained by the secondary K-feldspar lenses within chloritized biotite and micron-size patches of perthite in the albitized plagioclase. Mg presents a significant increase of +30% (Fig. 6). The Si content increases by about +17%, which agrees with the overall albitization of plagioclase (Fig. 6). Al released during albitization of plagioclase may have been consumed during chloritization of biotite and the formation of secondary K-feldspar. However, the albitization reflects an overall increase in Al of +7%. The Fe content remains stable (Fig. 6). The Fe released during chloritization of biotite was probably retained to form the secondary Fe-oxides. The amount of Ti decreased about -5% (Fig. 6), most of it probably released during chloritization of biotite and partly retained in secondary titanite. The variation in Mn shows a loss of -2% (Fig. 6). The loss of P was about -19% (Fig. 6), mostly due to the dissolution of monazite in the albitized profile. Some of the P participated in the formation of secondary fluorapatite in combination with F released during chloritization of biotite.

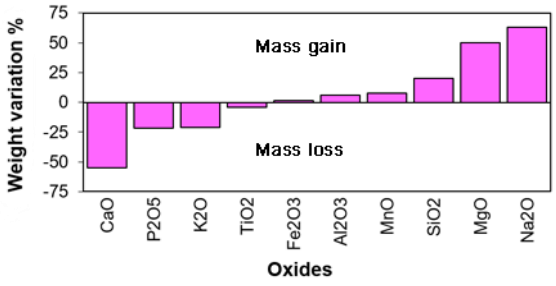

Fig. 6. Weight variation (%) diagram of the major elements in the red-stained albitized facies vs. unaltered rocks. Positive variation indicates an increase in the element concentration in the albitized facies with respect to the unaltered rocks.

$\delta^{18}O$ composition

Primary minerals in the unaltered rocks

The oxygen isotope compositions of primary feldspars and quartz were determined on unaltered leucogranite of the Guilleries Massif and porphyritic granite of the Roc de Frausa Massif and Hortmoier area (Fàbrega et al., 2016).

In the leucogranite of the Guilleries Massif, the zoned plagioclase has $\delta^{18}O$ values ranging from 8.52 to 9.51‰ in the Ca-bearing cores and 11.14 to 11.93‰ in the Na-rich rims (Table 4), showing a positive

correlation of $\delta^{18}O$ values with increasing sodic composition (Fig. 7a). Primary K-feldspar grains have $\delta^{18}O$ values ranging from 10.42 to 11.65‰ (Table 4), without any correlation with the primary K-feldspar composition (Fig. 7b). Primary quartz has a $\delta^{18}O$ composition between 6.4 and 9.60‰ (Table 4). In the Tagamanent area (see Fig. 2b), the $\delta^{18}O$ of the K-feldspar phenocrysts is between 10.6 and 10.8‰, close to the mean value of the primary matrix K-feldspar grains in the Guilleries samples.

Table 4. $\delta^{18}O$ (‰) of feldspars and quartz in the Guilleries and Roc de Frausa Massifs

	unaltered rock				red albitized rock		
massif	**plagioclase (core)**	**plagioclase (rim)**	**k-feldspar**	**quartz**	**albitized plagioclase**	**microclinized k-feldspar**	**CL-dark quartz**
Guilleries	8.5 – 9.5	11.1–11.9	10.4 – 11.7	6.4 – 9.6	10.3 - 11.6	11.8 – 13.8	*
Roc de Frausa	7.2 – 9.5	9.9 – 12.0	11.5 – 12.4	7.4	11.1 – 12.8	12.3 – 14	12.0

In the porphyritic granite of the Roc de Frausa Massif, $\delta^{18}O$ values for the primary plagioclase range between 7.18 and 9.45 in the Ca-rich cores and 9.88 to 11.94‰ in the Na-rich rims (Table 4), displaying a positive correlation of $\delta^{18}O$ values with the increase of sodium content (Fig. 7a). The primary K-feldspar grains in the granitic matrix have $\delta^{18}O$ values ranging from 11.50 to 12.39‰ (Table 4) and do not show any correlation with the K-feldspar composition (Fig. 7b). In the porphyritic granite of Hortmoier area, primary K-feldspar phenocrysts have steady $\delta^{18}O$ values ranging from 11.4 to 11.6‰, near the mean value of the primary matrix K-feldspar grains in the Roc de Frausa samples,

In the Guilleries, Roc de Frausa and Hormoier, the $\delta^{18}O$ compositions of the primary feldspars are consistent with high $\delta^{18}O$ crustal-derived magmas and follow the expected higher values in $\delta^{18}O$ composition in the alkali feldspars characterized by *Anorthite* $\delta^{18}O$ < *K-feldspar* ≈ *Albite* $\delta^{18}O$ (Bindeman, 2008).

The oxygen isotope fractionation between primary plagioclase and K-feldspar ($\Delta^{18}O_{Ab\text{-}Kfs}$) were about +0.5‰ and -0.5‰ for the Guilleries and Roc de Frausa, respectively, suggesting that, within error, primary feldspars formed under equilibrium conditions (Fig. 8a). The oxygen isotope fractionation between primary quartz and primary plagioclase ($\Delta^{18}O_{Qtz\text{-}Pl}$) are negative, with values about -3 and -4‰ for the Guilleries and Roc de Frausa, respectively (Fig. 8b). In the case of the quartz and primary K-feldspar ($\Delta^{18}O_{Qtz\text{-}Kfs}$) fractionation, values are also negative about -3 and -5‰ for the Guilleries and Roc de Frausa, respectively (Fig. 8c). These negative fractionation values of plagioclase and K-feldspar with

respect to quartz are reversed and indicate that the feldspars and quartz formed under disequilibrium conditions.

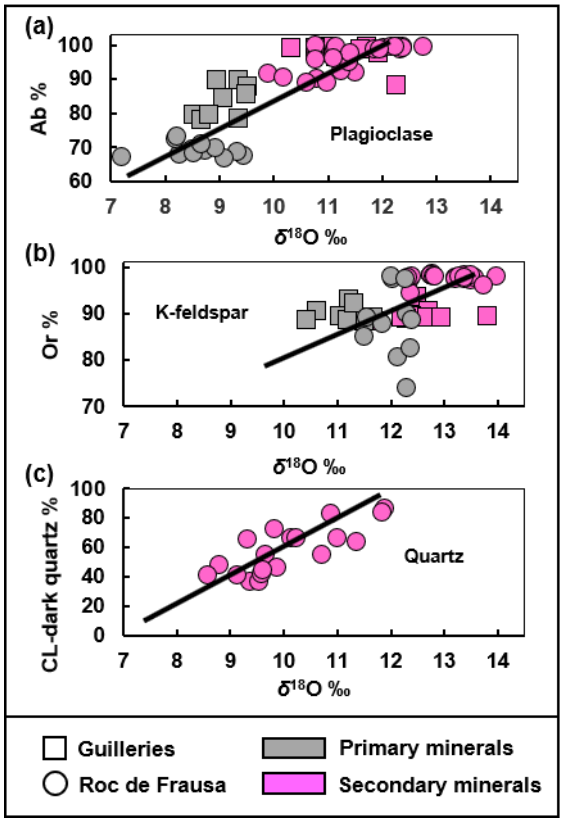

Figure 7. Plots of $\delta^{18}O$ values vs. mineral composition. **(a)** $\delta^{18}O$ values vs. plagioclase composition (Ab%). **(b)** $\delta^{18}O$ vs. K-feldspar composition (Or%). **(c)** $\delta^{18}O$ values vs. the percentage of CL-dark quartz estimated in the craters of quartz SIMS analyses. The $\delta^{18}O$ values of the primary and secondary CL-dark quartz correspond to the regression at 0 and 100%, respectively. These estimated values were rounded to the unit. Squares= Guilleries massif and circles = Roc de Frausa massif. Grey symbols = primary minerals and pink symbols = secondary minerals.

Secondary minerals of the red-stained albitized rocks

The $\delta^{18}O$ composition of the secondary feldspars and quartz of the red-stained rocks is higher than that for the respective primary phases, and significantly, each phase has similar values across the Guilleries and Roc de Frausa.

Albitized plagioclase from Guilleries has $\delta^{18}O$ ranging from 10.31 to 11.60‰ (Table 4), representing an average increase about +2‰ with respect to the $\delta^{18}O$ of the primary Ca-bearing plagioclase cores (Fig. 7a). At the Roc de Frausa, $\delta^{18}O$ values for albitized plagioclase range from 11.14 to 12.75 ‰ (Table 4), an average increase about +2.5‰ compared to the primary Ca-rich plagioclase cores (Fig. 7a).

475 The microclinized orthoclase of Guilleries has $\delta^{18}O$ values ranging from 11.76 to 13.81‰ (Table 4), an
476 average increase about +1.5‰ compared with the primary orthoclase (Fig. 7b). At Roc de Frausa, the
477 $\delta^{18}O$ composition of microclinized orthoclase ranges from 12.31 to 13.96‰ (Table 4), an average
478 increase about +1‰ compared to the primary orthoclase (Fig. 7b).

479 SEM-CL images of secondary quartz in Roc de Frausa samples showed that the SIMS craters presented a
480 mix of primary and secondary CL-dark quartz. The percentage of secondary CL-dark quartz was
481 estimated using CAD software and the $\delta^{18}O$ values were plotted against it and regressed to estimate the
482 $\delta^{18}O$ in both primary and CL-dark secondary quartz (Fig. 7c). Using this method, the primary quartz and
483 secondary CL-dark quartz were estimated to have $\delta^{18}O$ values of about 7.5‰ and 12‰, respectively
484 (Table 4), representing an estimated increase of about +4.5‰ for the secondary with respect to the
485 primary quartz.

486 The $\delta^{18}O$ values of secondary feldspars and quartz in both massifs indicate disequilibrium fractionation
487 values ($\Delta^{18}O$) for the mineral pairs. The oxygen isotope fractionation between secondary albite and
488 microclinized orthoclase ($\Delta^{18}O_{Ab2\text{-}Kfs2}$) presents disequilibrium values about -1.8‰ and -1.6‰ for the
489 Guilleries and Roc de Frausa, respectively (Fig. 8a). In the Roc de Frausa samples, the oxygen isotope
490 fractionation between CL-dark secondary quartz and albitized plagioclase ($\Delta^{18}O_{Qtz2\text{-}Ab2}$) is about 0.4‰
491 (Fig. 8b), and between CL-dark secondary quartz and microclinized orthoclase ($\Delta^{18}O_{Qtz2\text{-}Kfs2}$) is about -
492 1.2‰ (Fig. 8c).

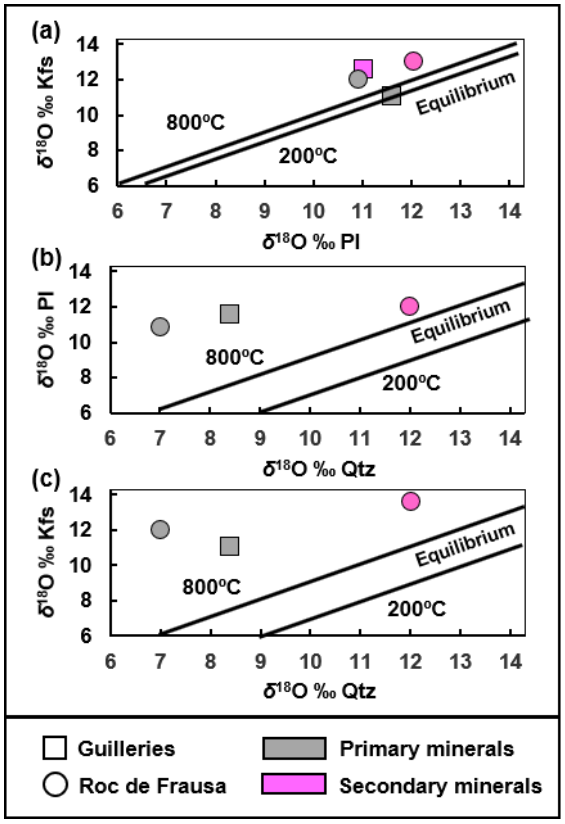

493

494 **Fig. 8.** *δ-δ* plots of primary and secondary mineral pairs of each massif. **(a)** Primary plagioclase vs. primary K-
495 feldspar and secondary albite vs. secondary microclinized K-feldspar. **(b)** Primary plagioclase vs. primary quartz
496 (grey) and albitized plagioclase vs. CL-dark quartz (pink). **(c)** Primary K-feldspar vs. primary quartz (grey) and
497 microclinized orthoclase vs. CL-dark quartz (pink). The equilibrium fractionations at equilibrium of each mineral pair
498 were calculated for 200 and 800 ºC using the equations of Zheng (1993).

499 # Geochronology

500 ## K-Ar dating of K-feldspar phenocrysts

501 K-Ar dating was carried out on K-feldspar phenocrysts collected in unaltered and red albitized rocks from
502 Hortmoier (see Fig. 2c). In unaltered rocks, the white primary orthoclase yielded a K-Ar age of
503 283 ± 10 Ma (2σ), which is consistent with the closure of the K-Ar system during magmatic cooling. Solé
504 et al. (2002) obtained similar $^{40}Ar/^{39}Ar$ ages of 276 and 269 Ma for primary orthoclase from the
505 Montnegre Massif (see Fig. 1) and considered them to register the time of magmatic cooling.

506 In the red albitized rocks, brown K-feldspar phenocrysts from albitized fracture walls (see Fig. 3e),
507 represent a degree of microclinization of 30-40% and yielded K-Ar ages of 244.5 ± 6, 237.6 ± 6, and
508 230.7 ± 6 Ma (2σ). The textural similarities and the overlapping of the three ages within the 2σ range

support a probable K-Ar resetting event during the Early Triassic. Given that these microclinized brown K-feldspar phenocrysts occur near the reaction front (see Fig. 3e) and are accompanied by partially albitized plagioclase and chloritized biotite, these Early Triassic dates are considered to constrain the age of the alteration in these red fracture facies in the lower part of the albitized profile.

In the same locality, the red albitized granite commonly has braided networks of millimetric calcite-filled fractures that cross-cut and thus post-date the albitized plagioclase, microclinized K-feldspar, chloritized biotite and altered quartz grains. K-feldspar phenocrysts in these samples, characterized by intense pink color, yielded K-Ar ages of 216.2 ± 6, 175.9 ± 5, 174.8 ± 5, and 164.0 ± 5 Ma (2σ). These Late Triassic-Early Jurassic ages may record an alteration that registers local resets of the K-Ar system relating to the formation of the calcite-filled fractures.

Monazite U-Th-Pb_{total} dating

EPMA U-Th-Pb_{total} dating was carried out on primary monazite grains in the unaltered rocks and on pseudomorphic secondary monazite associated with the reaction front in the red-stained albitized rocks. In the Guilleries Massif (Fig. 9a), the deconvolution of the histogram of the U-Th-Pb_{total} analyses (n = 117) yielded two significant ages of 251.2 ± 12 and 295.2 ± 14 Ma (2σ), with a relative misfit of 0.925. The histogram deconvolution of the analyses (n = 80) of the Roc de Frausa Massif (Fig. 9b) also indicates the existence of two significant ages of 254 ± 14 and 298 ± 12 Ma (2σ), presenting a relative misfit of 0.966.

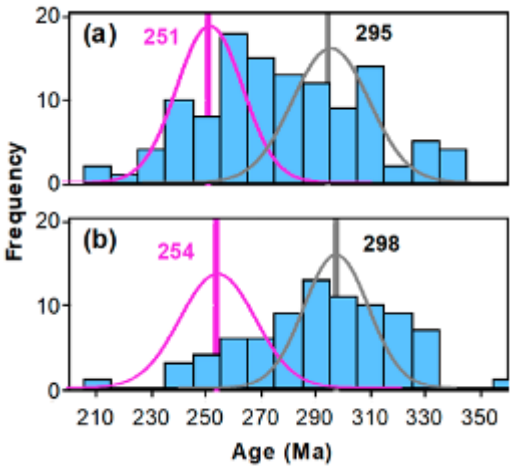

Fig. 9. Deconvoluted histograms of the U-Th-Pb_{total} monazite dates. **(a)** Guilleries Massif. **(b)** Roc de Frausa Massif. Grey vertical lines= Carboniferous – Permian ages. Pink vertical lines= Permian-Triassic ages. The two graphs **(a, b)** use the same X scale.

The distribution of the individual U-Th-Pb_{total} dates shows a clear relationship to the degree of albitization of the rock and the nature of the monazite grains. The analyses of primary monazite in the unaltered rocks systematically indicate Carboniferous-Permian dates, which are consistent, within error, with the ages of magmatic cooling of the granitoids reported by Martínez et al. (2008) and Aguilar et al. (2014) in the Guilleries and Roc de Frausa, respectively. These primary Carboniferous-Permian dates are also obtained in the relicts of primary monazite situated inside the monazite grains pseudomorphosed by secondary monazite (Fig. 10a). Differently, the analyses on the pseudomophic secondary monazite that formed in the albitized rocks near the reaction front (Fig. 10a, b, c, d) presented Permian-Triassic dates.

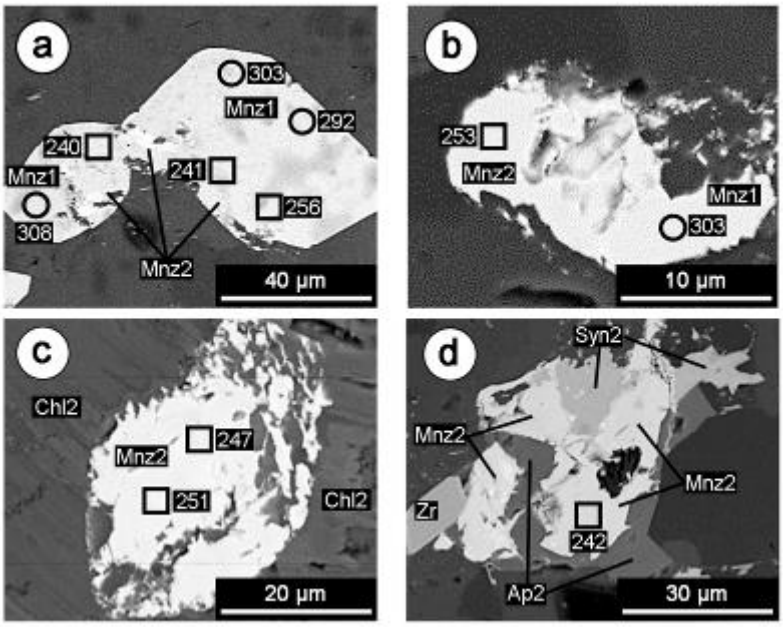

Fig. 10. BSE-images of monazite grains situated near the reaction front from the Guilleries Massif. Circles: position of U-Th-Pb_{total} analyses that yielded primary Carboniferous-Permian ages. Squares: position of U-Th-Pb_{total} analyses that yielded Permian-Triassic ages. **(a)** Euhedral and rounded grains of primary monazite with incipient secondary monazite in some of the external boundaries. **(b)** Monazite grain with primary and secondary domains. **(c)** Primary monazite grain completely pseudomorphosed by secondary monazite. **(d)** Monazite grain pseudomorphosed by monazite, apatite and synchysite and surrounded by euhedral synchysite and apatite. *Ap2: Secondary apatite; Chl2: chloritized biotite; Kfs2: Microclinized* orthoclase*; Mnz1: Primary monazite; Mnz2: Secondary pseudomorphic monazite; Qtz: Quartz; Syn2: secondary synchysite; Zr: zircon.*

Discussion

Age of the red-stained albitized profile

The microclinized orthoclase and secondary pseudomorphic monazite in the red-stained albitized rocks have K-Ar and U-Th-Pb ages around 240 and 250 Ma, respectively, indicating that the alteration probably developed between the Late Permian and the Early Triassic. The younger K-Ar ages for microclinized orthoclase may indicate ^{40}Ar loss during alteration because of the development of dislocation-rich microtextures like e.g., patchy perthites (Worden et al., 1990; Mark et al., 2008): the actual K-Ar age could be slightly older. Consistent with this possibility is the BSE observation that the dated K-feldspar phenocrysts have a significant component of patch perthite that could have acted as ^{40}Ar diffusion pathways. An alternative possibility is that the 240 Ma K-Ar age is geologically meaningful and that the alteration was ongoing in the red-stained upper part of the profile until 240 Ma, while the pseudomorphic monazite occurring at the lower albitization reaction front ceased earlier at around 250 Ma at depth. This does not accord with a common weathering profile evolution that becomes deeper with time, but in the Triassic geodynamic context, it may respond to a water table that rose in concert with the overall transgression.

The Permian-Triassic age of the alteration is also supported by preliminary studies of Early Triassic remagnetization of the secondary hematite and maghemite in the red-stained albitized profile of the Guilleries (Franke et al., 2010; Parcerisa et al., 2010a). The suggested age is also consistent with the capping of the red-stained albitized profile by Lower Triassic red-beds, clearly post-dating the alteration, in the southern area of the Guilleries Massif and the Tagamanent zone (see Fig. 2a, c).

All the age determinations using independent methods are coherent and point to the albitization and related alteration having developed during the Late Permian to Early Triassic, while the Variscan granites in NE Spain were exposed at the landsurface (López-Gómez et al., 2005; Linol et al., 2009; Galán-Abellán et al., 2013). Thus, the red-stained albitization relates to the Triassic palaeosurface, and its geopetal organization indicates that alteration of the granites most probably occurred under the influence of palaeogeography, climate, weathering, and groundwater.

$\delta^{18}O$ fluid-rock exchange during albitization

The minerals in both the unaltered and red albitized rocks have $\delta^{18}O$ values that implicate fluid-rock oxygen-isotope exchange processes during albitization. For example:

(1) All secondary phases in the red-stained albitized rocks (albitized plagioclase, microclinized orthoclase and CL-dark quartz) have higher $\delta^{18}O$ values compared to their primary counterparts in the unaltered rocks.

(2) The reactions follow this sequence: (a) albitization of plagioclase, (b) microclinization of orthoclase and (c) formation of CL-dark quartz, and partially overlapped over time. The $\delta^{18}O$ values of the secondary phases are in disequilibrium, suggesting that the minerals re-equilibrated with fluid with a changing $\delta^{18}O$ and/or temperature throughout the reaction sequence.

(3) The widespread and uniform character of the red-stained albitized rocks suggests that the alteration developed under long-lasting stable physico-chemical conditions, and that mineral reactions approached an equilibrium with oxygen isotopes in the fluid.

If the water-rock oxygen isotope exchange approaches equilibrium (i.e. forward and backward isotopic exchange occurs between the rock and fluid), the oxygen isotope composition of the fluid after re-equilibration with the rock (or a given mineral) can be estimated using a mass-balance equation (Taylor, 1977), by (Eq. 1):

$$\delta^{18}O_f^w = \delta^{18}O_i^w + \frac{R}{W} \times \left(\delta^{18}O_i^m - \delta^{18}O_f^m\right) \quad (1)$$

$\delta^{18}O^w_f$ and $\delta^{18}O^w_i$ being the initial and final oxygen isotope compositions of fluid, respectively, R and W the percentage of oxygen atoms in the rock (or mineral) and water, respectively, and $\delta^{18}O^m_i$ and $\delta^{18}O^m_f$ the oxygen isotope composition of the initial and final minerals, respectively.

Because the isotopic fractionation at equilibrium between minerals and fluid is also temperature dependent (Zheng and Hoefs, 1993), then the equilibrium temperature can be estimated using the oxygen isotope equilibrium equations of plagioclase (Eq. 2), K-feldspar (Eq. 3) and quartz (Eq. 4) with fluid, being (Zheng, 1993):

$$1000 \ln \alpha_{Ab-H2O} = \frac{4.33}{T^2} \times 10^6 - \frac{6.15}{T} \times 10^3 + 1.98 \quad (2)$$

$$1000 \ln \alpha_{Kfs-H2O} = \frac{4.32}{T^2} \times 10^6 - \frac{6.27}{T} \times 10^3 + 2.00 \quad (3)$$

$$1000 \ln \alpha_{Qtz-H2O} = \frac{4.48}{T^2} \times 10^6 - \frac{4.77}{T} \times 10^3 + 1.71 \quad (4)$$

Where T is the equilibrium temperature and $1000\ln\alpha \sim (\delta^{18}O^{m}_{f} - \delta^{18}O^{w}_{f})$ the oxygen isotope fractionation between mineral and fluid, being $\delta^{18}O^{w}_{f}$ determined by Eq. 1.

Initial $\delta^{18}O$ composition of fluids and R/W ratio

In fossil fluid-rock interactions, the initial oxygen isotope composition of the fluid, usually water, ($\delta^{18}O^{w}_{i}$) and the R/W ratio are usually unknown variables. This limitation makes it necessary to adopt reasonable $\delta^{18}O^{w}_{i}$ and R/W values to approach the final oxygen isotope composition of fluids and hence the equilibrium temperature of mineral and rock alteration. The geopetal structure of the red-stained profile beneath the Triassic unconformity suggests that the alteration was probably triggered by infiltrating Permian-Triassic surficial waters and groundwaters hosted in the Variscan granites. Groundwaters deep in the stable crystalline basements, typically at depths between several hundreds or thousands of meters, have $\delta^{18}O$ values between -8 and -12‰ (Kloppmann et al., 2002). This negative shifting of groundwater $\delta^{18}O$ is promoted by water-rock interaction reactions including the formation of kaolinite from dissolution of smectite and feldspars, and the precipitation of Fe-hydroxides (Kloppmann et al., 2002). These negative $\delta^{18}O$ values have been described worldwide in groundwaters in crystalline basements, including e.g., the European French Massif Central (Kloppmann et al., 2002), the Black Forest (Stober and Bucher, 1999a), the Alps (Barth, 2000) and the Fennoscandian and Ukrainian shields (Stober and Bucher, 1999b), the North American Canadian shield (Frape and Fritz, 1982, 1987; Frape et al., 1984a; Stober and Bucher, 1999b), the African Ahaggar Massif and Dodoma area (Nkotagu, 1996; Saighi et al., 2001), and the Indian Ranchi area (Saha et al., 2001), suggesting that negative $\delta^{18}O$ values are intrinsic of deep groundwater (Kloppmann et al., 2002). Assuming an analogy between the current and the Permian-Triassic granitic basement, negative $\delta^{18}O$ values between -8 and -12‰ can be reasonably assumed for the Permian-Triassic palaeogroundwater in the granitoids of the Guilleries and Roc de Frausa Massifs.

The rock to water (R/W) oxygen mass ratio is also a key factor for an estimation of the isotopic evolution of the fluid. Reactions arising directly at fracture walls, where solution may be renewed by circulation, may correspond to relative low R/W ratios, whereas those occurring away from the fractures, at the reaction front within primary crystals in an almost closed system, most likely correspond to higher R/W

ratios. To determine a minimum and conservative estimate of the $\delta^{18}O$ evolution of water, calculations were carried out applying R/W values of 0.5 and 1, considered to be high (≥1) water to rock ratios (Taylor, 1977).

δ^{18}O evolution in fluids and precipitation temperature

The $\delta^{18}O$ disequilibrium values of the secondary phases are indicative of either the $\delta^{18}O$ evolution of fluid or temperature variations during the alteration. Possible scenarios of $\delta^{18}O$ evolution in the fluids facilitating the albitization and related temperatures were explored using the reactions of albitization of plagioclase, microclinization of orthoclase and the formation of CL-dark quartz. The initial $\delta^{18}O_{im}$ and final $\delta^{18}O_{fm}$ oxygen isotope compositions of minerals applied in Eq. 1 for each reaction were, respectively, the averaged SIMS $\delta^{18}O$ values of primary plagioclase and albitized plagioclase, primary orthoclase and secondary microclinized orthoclase, and primary quartz and secondary CL-dark quartz. To overcome the uncertainty about the initial oxygen isotope composition of fluid and rock to fluid (R/W) oxygen atomic abundance ratio, calculations were undertaken with minimum and maximum range values to determine the influence of the different components and estimate the validity of the calculated temperatures. Temperature calculations were tested for initial oxygen isotope compositions of fluid ($\delta^{18}O_{if}$) of -8 and -12‰ and R/W in the range of 0.5 and 1.0 that might be consistent with fluid flow rate in the main fractures and in restricted cracks, respectively.

Equilibrium calculations were conducted with two options about fluid behaviour within the system.

(1) A closed system, in which fluid is retained in the system and where the reactions follow each another according to the sequence highlighted by petrographical relationships. The evolution of the oxygen isotope composition of the water was calculated across the sequence: albitization of plagioclase, microclinization of orthoclase and the formation of CL-dark quartz. The final oxygen isotope composition of fluid (Eq. 1) obtained in the previous reaction was the initial value in the next reaction. This option is relative to minimal chemical exchanges with the surrounding systems.

(2) An open system, in which fluid is renewed by circulation. The calculation (Eq. 1) considered concomitant mineral alterations and with the same initial fluid composition for each reaction. It corresponds to exchanges with surrounding systems, allowing imports and exports of chemical elements. After calculation of the resulting oxygen isotope composition of fluid for each reaction, the corresponding

654 temperatures were calculated using Eq. (2), (3) and (4) for albitization of plagioclase, microclinization of
655 K-feldspar and the CL-dark quartz formation, respectively.

656 The results of the calculations are summarized in Table 5 and call for a few remarks: (1) The
657 temperatures obtained for the Guilleries and Roc de Frausa massifs have very similar values, with an
658 averaged standard error in each reaction of about ±7ºC. (2) Calculated temperatures for the reactions
659 (Eq. 2, 3, 4) are higher if they were concomitant in an open system; (3) Calculated temperatures are
660 higher when considering a lower R/W oxygen mass ratio, i.e. more solution in the system; (4) There is a
661 systematic discrepancy in the calculated temperature with the various reactions: the lowest calculated
662 temperature is always for orthoclase microclinitisation and the highest for the precipitation of CL-dark
663 quartz. These discrepencies are attributed to interaction effects, like different rates between reactions or
664 fluid access to the minerals, and even shifts in the mineral isotope analyses. Whatever, the range of the
665 calculated temperatures remains relatively low about variation in the initial parameters. Increasing R/W
666 ratio from 0.5 to 1.0 lowers the calculated temperatures by about 10 to 20%. Lowering $\delta^{18}O$ in the initial
667 fluid from -8 to -12‰ lowers the calculated temperatures by about the same amount. Discrepencies
668 between the calculated temperature of microclinitisation of orthoclase and precipitation of CL-dark quartz
669 are of the same order of magnitude, about 25 - 30%. The maximum divergence between all the calculated
670 temperatures is 55°C, and the mean of all the calculated temperatures (if it makes sense) is 56.5 ± 15ºC
671 (1σ). The variation in the calculated temperatures seems to be relatively low, about the same as the
672 variation in the parameters introduced into the calculations, suggesting that evolution of the reaction fluid
673 can be considered, within its error estimation, as an isothermal process around 55ºC.

674 Regardless of the lack of precision, these values show that the temperatures of the reactions associated
675 with development of red-stained albitized rocks are significantly below temperatures suggested for
676 hydrothermal albitisation (Cathelineau, 1986; Boulvais et al., 2007) and tardi-magmatic alteration (Lee
677 and Parsons, 1997; Fiebig and Hoefs, 2002), and are consistent with shallow near-landsurface conditions.

678 **Table 5. $\delta^{18}O$ fluid evolution and reaction temperatures.** Regarding the indefinite alteration conditions,
679 temperature values are rounded to the unit.

mineral reaction	R/W oxygen mass ratio	initial $\delta^{18}O$ fluid ‰	final $\delta^{18}O$ fluid ‰	reaction temperature °C
sequential reactions # closed system				
albitization of plagioclase	0.5	-8.0	-9.0	72
	1.0	-8.0	-10.0	65
microclinization of orthoclase	0.5	-9.0	-9.7	56
	1.0	-10.0	-11.5	47
precipitation of CL-dark quartz	0.5	-9.7	-12.1	79
	1.0	11.5	-16.6	58
albitization of plagioclase	0.5	-12.0	-13	49
	1.0	-12.0	-14	44
microclinization of orthoclase	0.5	-13.0	-13.7	36
	1.0	-14.0	-15.5	36
precipitation of CL-dark quartz	0.5	-13.7	-16.1	58
	1.0	15.5	-20.2	39
concomitant reactions # open system				
albitization of plagioclase	0.5	-8.0	-9.0	72
	1.0	-8.0	-10.0	65
microclinization of orthoclase	0.5	-8.0	-8.7	62
	1.0	-8.0	-9.5	58
precipitation of CL-dark quartz	0.5	-8.0	-10.3	91
	1.0	-8.0	-12,6	77
albitization of plagioclase	0.5	-12.0	-13.0	49
	1.0	-12.0	-14.0	44
microclinization of orthoclase	0.5	-12.0	-12,7	41
	1.0	-12.0	-13.5	38
precipitation of CL-dark quartz	0.5	-12.0	-14.3	67
	1.0	-12.0	-16.6	55

680

681 ## Palaeoenvironmental setting of the albitization

682 The dating of albitization to the late Permian-early Triassic unquestionably constrains the alteration to the
683 Triassic palaeosurface that covers it. During the Late Permian-Early Triassic, northeastern Spain was
684 situated in subtropical latitude (López-Gómez et al., 2005; Scotese and Schettino, 2017). The transition
685 between Permian and Triassic times included a severe global warming described as an apocalyptic
686 greenhouse palaeoclimate (Erwin, 1993; Retallack, 1999; Sun et al., 2012), making life difficult in
687 equatorial latitudes (Brookfield, 2008; Joachimski et al., 2012). Land temperatures possibly approached
688 40°C and may have fluctuated to even higher temperatures (Joachimski et al., 2012; Sun et al., 2012).

689 In addition, Triassic palaeoenvironments are known for their giant salt deposits connected with lagunal
690 evaporitic environments (Hay et al., 2006; Brookfield, 2008; Bourquin et al., 2011) and the frequency of
691 halite moulds in transgressive epicontinental and continental clastic deposits (Courel, 1982; Galán-
692 Abellán and Martínez, 2018). It is possible that in continental settings halite may have been derived via

aeolian processes from marine-derived saline lakes and saltflats together with red desert dust typical of Triassic red sandstone deposits (Ruffell and Hounslow, 2006). Leaching of the salt accumulated in the landscape would have provided Na-rich solutions depleted in K relative to marine brines (Fig. 11a).

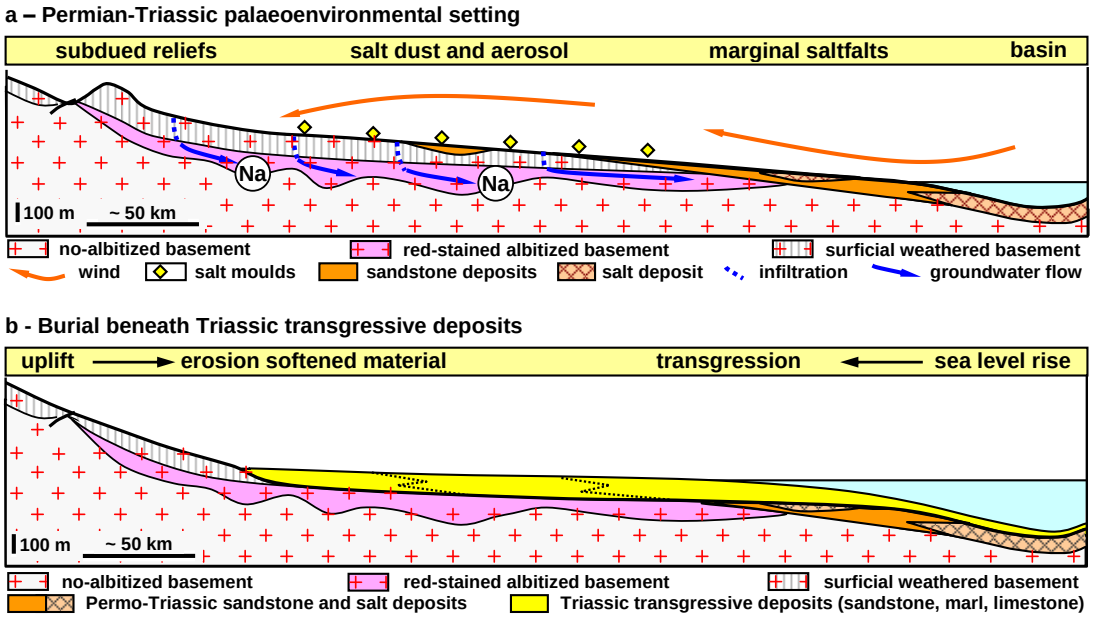

Fig. 11. Palaeoenvironmental settings during development of the red-stained albitized profiles. **(a)** Weathering mantles and saline environments of the postulated Triassic landscape with Na-enriched infiltrating waters and groundwater that probably triggered the formation of the albitized profiles. **(b)** Removal of the regolith mantle and burial of the albitized horizons by the Early Triassic transgression.

A geochemical mass balance for the studied Triassic red-stained albitized facies (Fig. 6) shows that albitization of plagioclase is triggered by an interaction between rock and Na-rich fluids with replacement of Ca by Na. Salt accumulated in the Triassic landscape is the most likely source of Na-rich solutions. For example, dense saline brines could have been a major contributor to the regional groundwater (Rogers and Dreiss, 1995; Wooding et al., 1997; Simmons et al., 2001) to depths of 1 km and more (Magri et al., 2009). The overall tectonic stability and subdued relief of the crystalline basement during the Permian-Triassic period (López-Gómez et al., 2005; Bourquin et al., 2011; Galán-Abellán et al., 2013) would have favoured slow groundwater flow rates, leading to long residence times and pervasive fluid/rock contact.

These unique settings of Triassic palaeogeography are considered to be responsible for the albitization of granitic rocks in Triassic landscapes that are recognized and dated in several basement massifs in Western Europe, i.e. French Massif Central affecting as well Carboniferous and Permian graben deposits (Yerle and Thiry, 1979; Schmitt et al., 1984; Clément, 1986; Schmitt, 1992), the Morvan Massif (Ricodel et al.,

713 2007; Parcerisa et al., 2010b), the Polish Sudetes (Yao et al., 2011; Yao 2013) and the Spanish Guilleries
714 and Roc de Frausa Massifs (Fàbrega et al., 2013; Franke et al., 2010).

715 A question remains about the depth at which the alteration leading to albitization occurred. Reaction
716 temperatures calculated from the oxygen isotope composition of minerals and hypotheses about the
717 oxygen isotope composition of reactant fluids and their circulation led to an estimate of the mean
718 temperature of albitization and associated reactions of about 55°C. Based on this temperature, an estimate
719 of the mean depth at which alteration occurred can be made by applying a geothermal gradient and a
720 surface temperature. A surficial temperature could be set to 30°C in consideration of the high
721 palaeotemperature proposed for the Permian-Triassic boundary (Retallack, 1999; Joachimski et al., 2012)
722 and a geothermal gradient for crystalline basement in a stable tectonic context could be set at about 25–
723 30°C/km. Under such conditions, albitization may have taken place at about 1 km depth.

724 This finding must include the possibility that a thick regolith existed between the surface and the
725 albitization zone. The geopetal architecture of the profile is a key characteristic, and the greater intensity
726 of alteration in the upper zones compared with the lesser intensity and more clearly fracture-controlled
727 alteration at depth, suggests a transition between a near-surface unconfined aquifer and a deeper fractured
728 rock aquifer system with restricted flow rate. If the albitized zone was surmounted by a regolith, high
729 hydraulic conductivity and seepage from the surface to depth would probably have prevailed. The upper
730 part of the profile may have been formed of loose weathered rocks, most likely sands with kaolinite
731 resulting from the weathering of feldspar, as suggested by Triassic sand deposits (Algeo and Twitchett,
732 2010; Benton and Newell, 2013). The nature of deeper horizons immediately overlying the albitized
733 zones is more difficult to comprehend. Long-lasting infiltration and seepage through these horizons may
734 have led to alteration of its most sensitive minerals, like Ca-plagioclase and biotite, deconstructed the
735 granite fabric and generated a relatively erodible arkosic grit. Given the extreme stability and long
736 persistence of Triassic palaeosurface the regolith cover may have reached 100, or even 300m in thickness.

737 This loose regolith material was later eroded, most probably during the period of relief rejuvenation and
738 intra-belt basin erosion during the Early Triassic (Bourquin et al., 2011) corresponding to the widespread
739 unconformity observed in the German Triassic (Trusheim, 1961; Wolburg, 1968; Röhling, 1991). Erosion
740 and burial beneath Triassic deposits was driven by tectonic activity and sea level rise (Fig. 11b).

Conclusions

A widespread and distinctive red stained and albitized granitic facies beneath the Triassic unconformity in NE Spain was formed in the Late Permian to Early Triassic based on three independent dating methods. This major result indicates that the albitization and associated alteration are related to the Triassic palaeosurface that unconformably overlies the albitized profile and developed in response to pervasive infiltrating fluid flow while the Variscan granites of NE Spain were exposed at the land surface.

$\delta^{18}O$ isotope data show that the secondary phases of the red-stained albitized facies (i.e. albitized plagioclase, microclinized orthoclase and CL-dark quartz) are $\delta^{18}O$ enriched with respect to their primary counterparts in unaltered rocks. Calculation of the oxygen isotope equilibrium temperature between minerals and albitizing fluids was undertaken by testing minima and maxima range values of initial oxygen isotope composition of fluid and rock to fluid mass ratios consistent with fluid flow rates in main and restricted fractures. This led to an estimate that albitized plagioclase, microclinized orthoclase and CL-dark quartz formed between 45 and 65°C. These temperatures are far less than 200 to 400ºC typically assigned to late-magmatic and hydrothermal albitization processes. Instead, the low temperature range accords with the geological settings and age dating that correlates the red-stained albitized profile with the Triassic palaeosurface. It is possible that the albitized profile may have developed a few hundred meters beneath the Triassic palaeosurface and was subsequently exposed at the surface after erosion of the uppermost weathering mantles.

Albitization resulted from Na accumulation triggered by Na-rich reactant solutions. The source of Na is considered to have been connected to the ubiquity of salt in the Triassic landscapes in the region, in lagunal and marginal salt flats as well as aeolian accumulations on extensive continental surfaces. A combination of surficial brines infiltrating groundwaters and a long period of tectonic stability could have facilitated pervasive alteration in 100 to 200 m deep profiles.

The significant amounts of secondary apatite formed during this alteration must be taken into account if fission track analysis or (U-Th)/He dating is carried out on these red-stained albitized rocks.

Acknowledgements

We would like to thank an anonymous reviewer and Douglas Elmore from University of Oklahoma, whose comments helped considerably to improve the focus of the paper. Authors are also indebted to

Tony Milnes from University of Adelaide for his revision and helpful comments, and for language edition, that strengthened the manuscript. Also, thanks to the technical staff of the Laboratorio General de Isotopos Estables of the Universidad de Salamanca (Spain) for the oxygen isotope CO_2-fluorination analyses and their useful technical comments. We wish to thank Dr. Xavier Llobet of the CCiTUB of the Universitat de Barcelona (Spain) for his technical support in the EPMA analyses of silicates and the U-Th-Pb_{total} monazite dating. Dr. Pura Alfonso, Escola Politècnica Superior d'Enginyeria de Manresa (Spain), for her support in analyzing EPMA data. Abigail Jiménez, from the Escola Politècnica Superior d'Enginyeria de Manresa (Spain), for the preparation of the epoxi mounts for EPMA monazite analyses. Dr. Marc Poujol, from Geosciences Rennes, Université de Rennes 1, for the ICP-MS U/Pb and Th/Pb dating of our monazite internal standard and for sharing with us his knowledge about monazite dating. This research was performed within the framework of DIHIME (CGL2015-66355-C2-1-R) and FEIBOB projects (PGC2018-093903-B-C22) of DGICYT, Ministerio de Economia y Competitividad, Gobierno de España and Grup Consolidat de Recerca "Geologia Sedimentària" (2017-SGR-824) and Grup de Recerca en Mineria Sostenible (2017-SGR-198) supported by the Comissionat per a Universitats i Recerca del Departament d'Empresa i Coneixement de la Generalitat de Catalunya.

Data Availability

The Electronic Supplementary Information related to this article can be obtained in the datasets:

[dataset] Parcerisa Duocastella, D. [et al.]. (2016). Geostandards of the Valentí Masachs Geology Museum [Dataset]. 1 v. Universitat Politècnica de Catalunya. DOI: 10.5821/data-2117-103444-1[https://upcommons.upc.edu/handle/2117/103444].

[dataset] Fàbrega, C. [et al.]. (2018). Geochemical data of albitized profiles in Europe [Dataset]. 1 v. Universitat Politècnica de Catalunya. DOI: 10.5821/data-2117-114114-1[https://upcommons.upc.edu/handle/2117/114114].

References

Aagaard P, Egeberg PK, Saigal GC (1990) Diagenetic albitization of detrital K-feldspars in Jurassic, Lower Cretaceous and Tertiary clastic reservoir rocks from offshore Norway; II, Formation water chemistry and kinetic considerations. J Sediment Res 60:575

Ague JJ, van Haren JLM (1996) Assessing metasomatic mass and volume changes using the bootstrap, with application to deep crustal hydrothermal alteration of marble. Econ Geol 91:1169–1182. doi: 10.2113/gsecongeo.91.7.1169

799 Aguilar C, Liesa M, Castineiras P, Navidad M (2014) Late Variscan metamorphic and magmatic
800 evolution in the eastern Pyrenees revealed by U-Pb age zircon dating. J Geol Soc London 171:181–
801 192. doi: 10.1144/jgs2012-086

802 Aguilar C, Liesa M, Štípská P, Schulmann K, Muñoz JA, Casas JM (2015) P-T-t-d evolution of orogenic
803 middle crust of the Roc de Frausa Massif (Eastern Pyrenees): a result of horizontal crustal flow and
804 Carboniferous doming? J Metamorph Geol 33:273–294. doi: 10.1111/jmg.12120

805 Algeo TJ, Twitchett RJ (2010) Anomalous Early Triassic sediment fluxes due to elevated weathering
806 rates and their biological consequences. Geol 38:1023–1026. doi: 10.1130/G31203.1

807 Anadón P, Cabrera L, Colombo F, Marzo M, Riba O (1986) Syntectonic Intraformational Unconformities
808 in Alluvial Fan Deposits, Eastern Ebro Basin Margins (NE Spain). In: Foreland Basins. Blackwell
809 Publishing Ltd., Oxford, UK, pp 259–271

810 Baker JH (1985) Rare earth and other trace element mobility accompanying albitization in a Proterozoic
811 granite, W. Bergslagen, Sweden. Mineral Mag 49:107–115. doi: 10.1180/minmag.1985.049.350.17

812 Barth SR (2000) Geochemical and boron, oxygen and hydrogen isotopic constraints on the origin of
813 salinity in groundwaters from the crystalline basement of the Alpine Foreland. Appl Geochemistry
814 15:937–952. doi: 10.1016/S0883-2927(99)00101-8

815 Battiau-Queney Y (1997) Preservation of old palaeosurfaces in glaciated areas: examples from the French
816 western Alps. Geol Soc London, Spec Publ 120:125–132. doi: 10.1144/GSL.SP.1997.120.01.08

817 Beinlich A, Klemd R, John T, Gao J (2010) Trace-element mobilization during Ca-metasomatism along a
818 major fluid conduit: Eclogitization of blueschist as a consequence of fluid–rock interaction.
819 Geochim Cosmochim Acta 74:1892–1922. doi: 10.1016/j.gca.2009.12.011

820 Benton MJ, Twitchett RJ (2003) How to kill (almost) all life: The end-Permian extinction event. Trends
821 Ecol Evol 18:358–365. doi: 10.1016/S0169-5347(03)00093-4

822 Bernet M, Bassett K (2005) Provenance Analysis by Single-Quartz-Grain SEM-CL/Optical Microscopy. J
823 Sediment Res. doi: 10.2110/jsr.2005.038

824 Bindeman I (2008) Oxygen Isotopes in Mantle and Crustal Magmas as Revealed by Single Crystal
825 Analysis. Rev Mineral Geochemistry 69:445–478. doi: 10.2138/rmg.2008.69.12

826 Boles JR (1982) Active albitization of plagioclase, Gulf Coast Tertiary. Am J Sci 282:165–180

827 Boulvais P, Ruffet G, Cornichet J, Mermet M (2007) Cretaceous albitization and dequartzification of
828 Hercynian peraluminous granite in the Salvezines Massif (French Pyrénées). Lithos 93:89–106

829 Bourquin S, Bercovici A, López-Gómez J, Diez JB, Broutin J, Ronchi A, Durand M, Arche A, Linol B,
830 Amour F (2011) The Permian-Triassic transition and the onset of Mesozoic sedimentation at the
831 northwestern peri-Tethyan domain scale: Palaeogeographic maps and geodynamic implications.
832 Palaeogeogr Palaeoclimatol Palaeoecol 299:265–280

833 Brookfield ME (2008) Palaeoenvironments and palaeotectonics of the arid to hyperarid intracontinental
834 latest Permian- late Triassic Solway basin (U.K.). Sediment Geol 210:27–47

835 Cathelineau M (1986) The hydrothermal alkali metasomatism effects on granitic rocks: Quartz
836 dissolution and related subsolidus changes. J Petrol 27:945–965

837 Cherniak DJ, Pyle JM (2008) Th diffusion in monazite. Chem Geol 256:52–61. doi:
838 10.1016/j.chemgeo.2008.07.024

Cherniak D., Watson EB, Grove M, Harrison TM (2004) Pb diffusion in monazite: a combined RBS/SIMS study. Geochim Cosmochim Acta 68:829–840. doi: 10.1016/j.gca.2003.07.012

Clément J.-Y. (1986) Minéralogie, pétrologie et géochimie du Permien de Lodève (Hérault, France). Diagenèse précoce, altération feldspathisante et mise en place des minéralisations uranifères. ENSMP, Mém Sci de la Terre 2: 136 p.

Cocherie A, Albarede F (2001) An improved U-Th-Pb age calculation for electron microprobe dating of monazite. Geochim Cosmochim Acta 65:4509–4522. doi: 10.1016/S0016-7037(01)00753-0

Cocherie A, Legendre O, Peucat JJ, Kouamelan AN (1998) Geochronology of polygenetic monazites constrained by in situ electron microprobe Th-U-total lead determination: Implications for lead behaviour in monazite. Geochim Cosmochim Acta. doi: 10.1016/S0016-7037(98)00171-9

Coombs DS (1954) The nature and alteration of some Triassic sediments from Southland, New Zealand. Trans R Soc New Zeal 82:65–109

Courel L (1982) Les facies de transgression du trias sur la bordure nord-est du Massif Central français. Geol Rundschau 71:773–781

Dinarès-Turell J, Diez JB, Rey D, Arnal I (2005) "Buntsandstein" magnetostratigraphy and biostratigraphic reappraisal from eastern Iberia: Early and Middle Triassic stage boundary definitions through correlation to Tethyan sections. Palaeogeogr Palaeoclimatol Palaeoecol 229:158–177. doi: 10.1016/j.palaeo.2005.06.036

Engvik AK, Putnis A, Fitz Gerald JD, Austrheim H (2008) Albitization of granitic rocks: the mechanism of replacement of oligoclase by albite. Can Mineral 46:1401–1415. doi: 10.3749/canmin.46.6.1401

Enrique P (1990) The Hercynian intrusive rocks of the Catalonian Coastal Ranges (NE Spain). Acta Geol Hisp 25:39–64

Erwin DH (1993) The great Paleozoic crisis: life and death in the Permian. Columbia University Press, New York, US

Fàbrega C, Parcerisa D, Gómez-Gras D (2013) Multiple Feldspar replacement in Hercynian granites of the Montseny-Guilleries Massif (Catalan Coastal Ranges, NE Spain). Geophys Res Abstr 15: EGU2013-7193–2

Fàbrega C, Parcerisa D, Gòmez-Gras D, Travé A, Franke C, Gurenko A (2016) Composició isotòpica de l'oxigen (18O/16O) en els feldspats i el quars dels granitoides hercinians: Guilleries-Montseny i Pirineus Orientals. In: Vilà M, Herms I, Cirés J (eds) Geoquímica ambiental a Catalunya. Recull d'articles. Monografies tècniques de l'Institut Cartogràfic i Geològic de Catalunya, núm. 5. Institut Cartogràfic i Geològic de Catalunya, Barcelona, Spain, pp 83–95 (**in Catalan**)

Fàbrega C, Parcerisa D, Rossell JM, Gurenko A, Franke C (2017) Predicting instrumental mass fractionation (IMF) of stable isotope SIMS analyses by response surface methodology (RSM). J Anal At Spectrom 32:731–748. doi: 10.1039/C6JA00397D

Fàbrega C, Parcerisa D, Gómez-Gras D, Travé A, Thiry M, Franke C, Gurenko A, Solé J (2018) Geochemical data of albitized profiles in Europe [Dataset] URL: https://upcommons.upc.edu/handle/2117/102354

Fallourd S, Poujol M, Boulvais P, Paquette JL, de Saint Blanquat M, Rémy P (2014) In situ LA-ICP-MS U-Pb titanite dating of Na-Ca metasomatism in orogenic belts: The North Pyrenean example. Int J Earth Sci 103:667–682

880 Fiebig J, Hoefs J (2002) Hydrothermal alteration of biotite and plagioclase as inferred from intragranular
881 oxygen isotope- and cation-distribution patterns. Eur J Mineral 14:49–60. doi: 10.1127/0935-
882 1221/2002/0014-0049

883 Franke C, Thiry M, Gómez-Gras D, Jelenska M, Kodzialko-Hofmokl M, Lagroix F, Parcerisa D, Spassov
884 S, Szuszkiewicz A, Turniak K (2010) Paleomagnetic age constrains and magneto-mineralogic
885 implications for the Triassic paleosurface in Europe. Geophys Res Abstr 12: EGU2010-7858

886 Frape SK, Fritz P (1982) The chemistry and isotopic composition of saline groundwaters from the
887 Sudbury Basin, Ontario. Can J Earth Sci 19:645–661. doi: 10.1139/e82-053

888 Frape SK, Fritz P (1987) Geochemical trends for groundwaters from the Canadian Shield. In: Saline
889 water and gases in crystalline rocks. Ottawa: Geological Association of Canada, pp 19–38

890 Frape SK, Fritz P, Blackmer AJ (1984) Saline groundwater discharges from crystalline rocks near
891 Thunder Bay. In: Ontario, Canada: International Symposium on Hydrochemical Balances of
892 Freshwater Systems, Upsala, Sweden. pp 369–379

893 Galán-Abellán AB, Martínez-Frías J (2018) Environmental conditions of E Iberia's Early Triassic: an
894 Earth example for understanding the habitability of ancient Mars. Episodes 41:33–50. doi:
895 10.18814/epiiugs/2018/v41i1/018004

896 Galán-Abellán B, López-Gómez J, Barrenechea JF, Marzo M, de la Horra R, Arche A (2013) The
897 beginning of the Buntsandstein cycle (Early–Middle Triassic) in the Catalan Ranges, NE Spain:
898 Sedimentary and palaeogeographic implications. Sediment Geol 296:86–102. doi:
899 10.1016/j.sedgeo.2013.08.006

900 Gómez-Gras D (1993) El Permotría de la Cordillera Costero Catalana: Facies y Petrología Sedimentaria
901 (Parte I). Boletín Geológico y Min España 104:115–161

902 Gómez-Gras D, Roigé M, Fondevilla V, Oms O, Boya S, Remacha E (2016) Provenance constraints on
903 the Tremp Formation paleogeography (southern Pyrenees): Ebro Massif VS Pyrenees sources.
904 Cretac Res 57:414–427. doi: 10.1016/j.cretres.2015.09.010

905 Hall MM, Veeraraghavan VG, Rubin H, Winchell PG (1977) The approximation of symmetric X-ray
906 peaks by Pearson type VII distributions. J Appl Crystallogr 10:66–68. doi:
907 10.1107/S0021889877012849

908 Hamilton M, Elmore D, Weaver B, Dulin S, Suneson NH (2014) Petrology and paleomagnetism of the
909 Long Mountain Granite, Wichita Mountains, Oklahoma. Igneous Rocks of the Southern Oklahoma
910 Aulacogen: Oklahoma. Geological Survey Guidebook 38: 319-326

911 Hamilton EM, Elmore RD, Weaver BL, Dulin S, Jackson J (2016) Paleomagnetic and petrologic study of
912 the age, origin, and significance of early and late Paleozoic events in the Long Mountain Granite,
913 Wichita Mountains, Oklahoma. GSA Bull 128: 187-202

914 Harlov DE, Wirth R, Hetherington CJ (2011) Fluid-mediated partial alteration in monazite: The role of
915 coupled dissolution-reprecipitation in element redistribution and mass transfer. Contrib to Mineral
916 Petrol. doi: 10.1007/s00410-010-0599-7

917 Hay WW, Migdisov A, Balukhovsky AN, Wold CN, Flögel S, Söding E (2006) Evaporites and the
918 salinity of the ocean during the Phanerozoic: Implications for climate, ocean circulation and life.
919 Palaeogeogr Palaeoclimatol Palaeoecol 240:3–46

920 Jamtveit B, Putnis C V, Malthe-Sørenssen A (2009) Reaction induced fracturing during replacement
921 processes. Contrib Mineral Petrol 157:127–133. doi: 10.1007/s00410-008-0324-y

922 Joachimski MM, Lai X, Shen S, Jiang H, Luo G, Chen B, Chen J, Sun Y (2012) Climate warming in the
923 latest Permian and the Permian-Triassic mass extinction. Geology 40:195–198. doi:
924 10.1130/G32707.1

925 Julivert M, Durán H (1990) Paleozoic stratigraphy of the Central and Northern part of the Catalonian
926 Coastal Ranges (NE Spain). Acta Geol Hisp 25:3–12

927 Kastner M, Siever R (1979) Low temperature feldspars in sedimentary rocks. Am J Sci 279:435–479

928 Kloppmann W, Girard J-P, Négrel P (2002) Exotic stable isotope compositions of saline waters and
929 brines from the crystalline basement. Chem Geol 184:49–70. doi: 10.1016/S0009-2541(01)00352-7

930 Lee MR, Parsons I (1997) Dislocation formation and albitization in alkali feldspars from the Shap granite.
931 Am Mineral. doi: 10.2138/am-1997-5-616

932 Linol B, Bercovici A, Bourquin S, Diez JB, López-Gómez J, Broutin J, Durand M, Villanueva-Amadoz U
933 (2009) Late Permian to Middle Triassic correlations and palaeogeographical reconstructions in
934 south-western European basins: New sedimentological data from Minorca (Balearic Islands, Spain).
935 Sediment Geol 220:77–94. doi: 10.1016/j.sedgeo.2009.06.003

936 López-Gómez J, Arche A, Marzo M, Durand M (2005) Stratigraphical and palaeogeographical
937 significance of the continental sedimentary transition across the Permian-Triassic boundary in
938 Spain. Palaeogeogr Palaeoclimatol Palaeoecol 229:3–23

939 Ludwig KR (2003) User's Manual for Isoplot 3.00 - A Geochronological Toolkit for Microsoft Excel.
940 Berkeley Geochronol Cent Spec Publ Special Pu:25–32

941 Magri F, Bayer U, Pekdeger A, Otto R, Thomsen C, Maiwald U (2009) Salty groundwater flow in the
942 shallow and deep aquifer systems of the Schleswig–Holstein area (North German Basin).
943 Tectonophysics 470:183–194. doi: 10.1016/j.tecto.2008.04.019

944 Mark DF, Kelley SP, Lee MR, Parnell J, Sherlock SC, Brown DJ (2008) Ar–Ar dating of authigenic K-
945 feldspar: Quantitative modelling of radiogenic argon-loss through subgrain boundary networks.
946 Geochim Cosmochim Acta 72:2695–2710. doi: 10.1016/j.gca.2008.03.018

947 Martínez FJ, Reche J, Iriondo A (2008) U–Pb Shrimp-RG zircon ages of Variscan igneous rocks from the
948 Guilleries massif (NE Iberia pre-Mesozoic basement). Geological implications. Comptes Rendus
949 Geosci 340:223–232. doi: 10.1016/j.crte.2007.12.006

950 Morad S, Bergan M, Knarud R, Nystuen JP (1990) Albitization of detrital plagioclase in Triassic
951 reservoir sandstones from the Snorre Field, Norwegian North Sea. J Sediment Petrol 60:411–425

952 Morad S, El-Ghali MAK, Caja MA, Sirat M, Al-Ramadan K, Mansurbeg H (2010) Hydrothermal
953 alteration of plagioclase in granitic rocks from Proterozoic basement of SE Sweden. Geol J 45:105–
954 116

955 Nkotagu H (1996) Application of environmental isotopes to groundwater recharge studies in a semi-arid
956 fractured crystalline basement area of Dodoma, Tanzania. J African Earth Sci 22:443–457. doi:
957 10.1016/0899-5362(96)00022-X

958 Oms O, Dinarès-Turell J, Vicens E, Estrada R, Vila B, Galobart A, Bravo AM (2007) Integrated
959 stratigraphy from the Vallcebre Basin (southeastern Pyrenees, Spain): New insights on the
960 continental Cretaceous−Tertiary transition in southwest Europe. Palaeogeogr Palaeoclimatol
961 Palaeoecol 255:35–47. doi: 10.1016/j.palaeo.2007.02.039

962 Parcerisa D, Casas L, Franke C, Gómez-Gras D, Lacasa G, Núñez JA, Thiry M (2010a)
963 Geomorphological stability of Permo-Triassic albitized profiles - case study of the Montseny-
964 Guilleries High (NE Iberia). Geophys Res Abstr 12: EGU2010-15607

965 Parcerisa D, Thiry M, Schmitt JM (2010b) Albitisation related to the Triassic unconformity in igneous
966 rocks of the Morvan Massif (France). Int J Earth Sci 99:527–544. doi: 10.1007/s00531-008-0405-1

967 Parcerisa D, Franke C, Fàbrega C, Yao K, Thiry M (2013), Implications from paleomagnetic age
968 constrains and petrology analyses on the reconstruction of the Triassic paleosurface in Europe –
969 examples from Catalonia and the Polish Sudetes, Abstract GP12A-02 presented at 2013 Fall
970 Meeting, AGU, San Francisco, Calif., US, 9-13 Dec.

971 Parcerisa D, Fàbrega C, Gurenko A, Franke C (2016) Geostandards of the Valentí Masachs Geology
972 Museum [Dataset] URL: https://upcommons.upc.edu/handle/2117/103444

973 Parrish RR (1990) U–Pb dating of monazite and its application to geological problems. Can J Earth Sci.
974 doi: 10.1139/e90-152

975 Parsons I, Lee MR (2009) Mutual replacement reactions in alkali feldspars I: microtextures and
976 mechanisms. Contrib to Mineral Petrol 157:641–661. doi: 10.1007/s00410-008-0355-4

977 Parsons I, Magee CW, Allen CM, Shelley JMG, Lee MR (2009) Mutual replacement reactions in alkali
978 feldspars II: trace element partitioning and geothermometry. Contrib to Mineral Petrol 157:663–687

979 Perez R, Boles JR (2005) An empirically derived kinetic model for albitization of detrital plagioclase. Am
980 J Sci 305:312–343

981 Petersson J, Eliasson T (1997) Mineral evolution and element mobility during episyenitization
982 (dequartzification) and albitization in the postkinematic Bohus granite, southwest Sweden. Lithos
983 42:123–146

984 Petersson J, Stephens MB, Mattsson H, Möller C (2012) Albitization and quartz dissolution in
985 Paleoproterozoic metagranite, central Sweden - Implications for the disposal of spent nuclear fuel in
986 a deep geological repository. Lithos 148:10–26. doi: 10.1016/j.lithos.2012.06.001

987 Petersson J, Fallick AE, Broman C, Eliasson T (2014) Imprints of multiple fluid regimes on episyenites in
988 the Bohus granite, Sweden. Lithos 196–197:99–114

989 Plümper O, Putnis A (2009) The Complex Hydrothermal History of Granitic Rocks: Multiple Feldspar
990 Replacement Reactions under Subsolidus Conditions. J Petrol 50:967–987. doi:
991 10.1093/petrology/egp028

992 Poujol M, Boulvais P, Kosler J (2010) Regional-scale Cretaceous albitization in the Pyrenees: evidence
993 from in situ U-Th-Pb dating of monazite, titanite and zircon. J Geol Soc London 167:751–767. doi:
994 10.1144/0016-76492009-144

995 Putnis A (2002) Mineral replacement reactions: from macroscopic observations to microscopic
996 mechanisms. Mineral Mag 66:689–708

997 Putnis A (2009) Mineral Replacement Reactions. Rev Mineral Geochemistry 70:87–124. doi:
998 10.2138/rmg.2009.70.3

999 Putnis A, Hinrichs R, Putnis CV, Golla-Schindler U, Collins LG (2007) Hematite in porous red-clouded
1000 feldspars: Evidence of large-scale crustal fluid-rock interaction. Lithos 95:10–18

1001 Ramseyer K, Boles JR, Lichtner PC (1992) Mechanism of plagioclase albitization. J Sediment Petrol
1002 62:349–456

1003 Retallack GJ (1999) Postapocalyptic greenhouse paleoclimate revealed by earliest Triassic paleosols in
1004 the Sydney Basin, Australia. Geol Soc Am Bull 111:52–70

1005 Ricordel C, Parcerisa D, Thiry M, Moreau MG, Gómez-Gras D (2007) Triassic magnetic overprints
1006 related to albitization in granites from the Morvan massif (France). Palaeogeogr Palaeoclimatol
1007 Palaeoecol 251:268–282. doi: 10.1016/j.palaeo.2007.04.001

1008 Roberts MP, Pin C, Clemens JD, Paquette JL (2000) Petrogenesis of Mafic to Felsic Plutonic Rock
1009 Associations: the Calc-alkaline Querigut Complex, French Pyrenees. J Petrol 41:809–844. doi:
1010 10.1093/petrology/41.6.809

1011 Rogers DB, Dreiss SJ (1995) Saline groundwater in Mono Basin, California: 1. Distribution. Water
1012 Resour Res 31:3131–3150. doi: 10.1029/95WR02108

1013 Röhling, H.G. (1991) A lithostratigraphic subdivision of the Lower Triassic in the Northwest German
1014 Lowlands and the German sector of the North Sea, based on gamma-ray and sonic logs. Geol Jb
1015 A119: 3–24.

1016 Røyne A, Jamtveit B, Mathiesen J, Malthe-Sørenssen A (2008) Controls on rock weathering rates by
1017 reaction-induced hierarchical fracturing. Earth Planet Sci Lett 275:364–369. doi:
1018 10.1016/j.epsl.2008.08.035

1019 Ruffell A, Hounslow M (2006) Triassic: seasonal rivers, dusty deserts and saline lakes. In: Rawson PF,
1020 Brenchley P (eds) The Geology of England & Wales. Geological Society of London, pp 295–325

1021 Rusk BG (2006) Intensity of quartz cathodoluminescence and trace-element content in quartz from the
1022 porphyry copper deposit at Butte, Montana. Am Mineral 91:1300–1312. doi:
1023 10.2138/am.2006.1984

1024 Rusk B, Reed M (2002) Scanning electron microscope–cathodoluminescence analysis of quartz reveals
1025 complex growth histories in veins from the Butte porphyry copper deposit, Montana. Geology
1026 30:727. doi: 10.1130/0091-7613(2002)030<0727:SEMCAO>2.0.CO;2

1027 Saha D, Dwivedi SN, Roy GK, Reddy D V. (2013) Isotope-based investigation on the groundwater flow
1028 and recharge mechanism in a hard-rock aquifer system: the case of Ranchi urban area, India.
1029 Hydrogeol J 21:1101–1115. doi: 10.1007/s10040-013-0974-3

1030 Saigal GC, Morad S, Bjørlykke K, Egeberg PK, Aagaard P (1988) Diagenetic albitization of detrital K-
1031 feldspar in Jurassic, Lower Cretaceous, and Tertiary clastic reservoir rocks from offshore Norway,
1032 I. Textures and origin. J Sediment Petrol 58:1003–1013

1033 Saighi O, Michelot JL, Filly A (2001) Isotopic characteristic of meteoric water and groundwater in
1034 Ahaggar massif (central Sahara)

1035 Schmitt JM (1986) Albitisation triasique, hydrothermalisme jurassique et altération supergène récente:
1036 métallogénie des gisements uranifères du Rouergue. Louis Pasteur University

1037 Schmitt JM (1992) Triassic albitization in southern France: an unusual mineralogical record from a major
1038 continental paleosurface. In: Schmitt JM, Gall Q (eds) Mineralogical and geochemical records of
1039 paleoweathering. Paris, ENSMP, Mem Sci Terre. ENSMP, Mémories des Sciences de la Terre,
1040 Paris, pp 115–131

1041 Schmitt JM, Baubron JC, Bonhomme MG (1984) Pétrographie et datations K-Ar des transformations
1042 minérales affectant le gîte uranifère de Bertholène (Aveyron-France). Miner Depos 19:123–131

1043 Scotese CR, Schettino A (2017) Late Permian-Early Jurassic Paleogeography of Western Tethys and the
1044 World. In: Soto J, Flinch J, Tari G (eds) Permo-Triassic Salt Provinces of Europe, North Africa and
1045 the Atlantic Margins. Elsevier, pp 57–95

1046 Simmons CT, Fenstemaker TR, Sharp JM (2001) Variable-density groundwater flow and solute transport
1047 in heterogeneous porous media: approaches, resolutions and future challenges. J Contam Hydrol
1048 52:245–275. doi: 10.1016/S0169-7722(01)00160-7

1049 Simon-Coinçon R (1999) Palaeolandscape reconstruction of the south-western Massif Central (France).
1050 Palaeoweathering, Palaeosurfaces Relat. Cont. Depos. 27:225–243

1051 Solé de Porta, N., Calvet, F., Torrentó L (1987) Análisis Palinologico del Triassico de los Catalanides
1052 (NE España). Cuad Geol Ibérica 11:237–254

1053 Solé J (2009) Determination of K-Ar ages in milligram samples using an infrared laser for argon
1054 extraction. Rapid Commun Mass Spectrom 23:3579–3590. doi: 10.1002/rcm.4280

1055 Solé J, Enrique P (2001) X-ray fluorescence analysis for the determination of potassium in small
1056 quantities of silicate minerals for K-Ar dating. Anal Chim Acta. doi: 10.1016/S0003-
1057 2670(01)01060-1

1058 Solé J, Cosca M, Sharp Z, Enrique P (2002) 40Ar/39Ar geochronology and stable isotope geochemistry
1059 of Late-Hercynian intrusions from north-eastern Iberia with implications for argon loss in K-
1060 feldspar. Int J Earth Sci 91:865–881

1061 Steiger RH, Jäger E (1977) Subcommission on geochronology: Convention on the use of decay constants
1062 in geo- and cosmochronology. Earth Planet Sci Lett 36:359–362. doi: 10.1016/0012-
1063 821X(77)90060-7

1064 Stober I, Bucher K (1999a) Origin of salinity of deep groundwater in crystalline rocks. Terra Nov
1065 11:181–185. doi: 10.1046/j.1365-3121.1999.00241.x

1066 Stober I, Bucher K (1999b) Deep groundwater in the crystalline basement of the Black Forest region.
1067 Appl Geochemistry 14:237–254. doi: 10.1016/S0883-2927(98)00045-6

1068 Sun Y, Joachimski MM, Wignall PB, Yan C, Chen Y, Jiang H, Wang L, Lai X (2012) Lethally Hot
1069 Temperatures During the Early Triassic Greenhouse. Science (80-) 338:366–370. doi:
1070 10.1126/science.1224126

1071 Suzuki K, Adachi M (1994) Middle Precambrian detrital monazite and zircon from the hida gneiss on
1072 Oki-Dogo Island, Japan: their origin and implications for the correlation of basement gneiss of
1073 Southwest Japan and Korea. Tectonophysics 235:277–292. doi: 10.1016/0040-1951(94)90198-8

1074 Suzuki K, Adachi M, Tanaka T (1991) Middle precambrian provenance of Jurassic sandstone in the Mino
1075 Terrane, central Japan: Th-U-total Pb evidence from an electron microprobe monazite study.
1076 Sediment Geol 75:141–147. doi: 10.1016/0037-0738(91)90055-I

1077 Suzuki K, Adachi M, Kajizuka I (1994) Electron microprobe observations of Pb diffusion in
1078 metamorphosed detrital monazites. Earth Planet Sci Lett 128:391–405. doi: 10.1016/0012-
1079 821X(94)90158-9

1080 Taylor HP (1977) Water/rock interactions and the origin of H2O in granitic batholiths: Thirtieth William
1081 Smith lecture. J Geol Soc London 133:509–558. doi: 10.1144/gsjgs.133.6.0509

1082 Thiry M, Schmitt JM, Simon-Coinçon R (1999) Problems, progress and future research concerning
1083 palaeoweathering and palaeosurfaces. In: Thiry M, Simon-Coinçon R (eds) Palaeoweathering,

Palaeosurfaces and Related Continental Deposits. Blackwell Science. Special Publications of the International Association of Sedimentologists, Oxford, pp 3–17

Thiry M, Théveniaut H, Simon-Coinçon R, Prognon C, Lenoir F, Lagroix F (2014) Persistent paléosurfaces in the basement of French Massif Central: geodynamic implications. In: Diagénèse: avancées récentes et perspectives. Association des Sédimentologistes Français (ASF), Orsay (France), pp 113–117

Trusheim, F. (1961) Über Diskordanzen im mitlleren Buntsandstein Norddeutschlands zwischen Weser und Ems. Erdöl-Zeitschrift 77: 361–367.

Vilà M, Pin C, Enrique P, Liesa M (2005) Telescoping of three distinct magmatic suites in an orogenic setting: Generation of Hercynian igneous rocks of the Albera Massif (Eastern Pyrenees). Lithos 83:97–127. doi: 10.1016/j.lithos.2005.01.002

Williams ML, Jercinovic MJ, Goncalves P, Mahan K (2006) Format and philosophy for collecting, compiling, and reporting microprobe monazite ages. Chem Geol 225:1–15. doi: 10.1016/j.mce.2005.09.009

Williams ML, Jercinovic MJ, Harlov DE, Budzyń B, Hetherington CJ (2011) Resetting monazite ages during fluid-related alteration. Chem Geol. doi: 10.1016/j.chemgeo.2011.01.019

Witkowski FW, Blundell DJ, Gutteridge P, Horbury AD, Oxtoby NH, Qing H (2000) Video cathodoluminescence microscopy of diagenetic cements and its applications. Mar Pet Geol 17:1085–1093. doi: 10.1016/S0264-8172(00)00055-6

Wojdyr M (2010) Fityk: a general-purpose peak fitting program. J Appl Crystallogr 43:1126–1128. doi: 10.1107/S0021889810030499

Wolburg, J. (1968) Vom zyklischen Aufbau des Buntsandsteins. Neues Jb Geol. Paläontol. Mh. 9: 535–559.

Wooding RA, Tyler SW, White I (1997) Convection in groundwater below an evaporating Salt Lake: 1. Onset of instability. Water Resour Res 33:1199–1217. doi: 10.1029/96WR03533

Worden RH, Walker FDL, Parsons I, Brown WL (1990) Development of microporosity, diffusion channels and deuteric coarsening in perthitic alkali feldspars. Contrib to Mineral Petrol 104:507–515. doi: 10.1007/BF00306660

Yao KFE (2013) Albitization and oxidation of the granitoïd rocks related to the Triassic paleosurface in the Sudetes (SW Poland). École Nationale Supérieure des mines de Paris

Yao KFE, Franke C, Thiry M, Paweł A, Szuszkiewicz A, Turniak K (2011) Albitization as record of the Triassic Paleosurface in the Sudetic Crystalline basement (Poland). Geophys Res Abstr 13: EGU2011-5930

Yerle JJ, Thiry M (1979) Albitisations et minéralisations uranifères dans le socle et les sédiments permo-houillers du bassin de Brousse-Broquiés (Aveyron, France). Bull du BRGM Ser 2 4:275–290

Zheng Y-F, Hoefs J (1993) Carbon and oxygen isotopic covariations in hydrothermal calcites. Miner Depos 28. doi: 10.1007/BF00196332

Zheng Y-F (1993) Calculation of oxygen isotope fractionation in anhydrous silicate minerals. Geochim Cosmochim Acta 57:1079–1091. doi: 10.1016/0016-7037(93)90042-U